GEOPHYSICS®

Repeatability of high-resolution 3D seismic data

Journal:	*Geophysics*
Manuscript ID	GEO-2018-0099.R2
Manuscript Type:	Technical Paper
Keywords:	4D, high-resolution, shallow, time-lapse, processing
Area of Expertise:	Seismic Data Acquisition, Signal Processing

REPEATABILITY OF HIGH-RESOLUTION 3D SEISMIC DATA

Malin Waage[1], Stefan Bünz[1], Martin Landrø[2], Andreia Plaza-Faverola[1], Kate A. Waghorn[1]

Right Running Head: **High-resolution 4D seismic data**

[1]CAGE – Centre for Arctic Gas Hydrates, Environment and Climate, Department of Geosciences, UiT the Arctic University of Norway, N-9037 Tromsø, Norway. E-mail: malin.waage@uit.no, stefan.bunz@uit.no, andreia.a.faverola@uit.no, kate.a.waghorn@uit.no.

[2] NTNU - Norwegian University of Science and Technology, Department of Electronic Systems, 7491 Trondheim, Norway. E-mail: martin.landro@ntnu.no.

Original paper date of submission: 05-Feb-2018

Revised paper date of submission: 11-Oct-2018

ABSTRACT

High-resolution 4D (HR4D) seismic data has a potential for improving the current state-of-art in detecting shallow (≤500-1000 m below seafloor) subsurface changes on a very fine scale (~3-6 m). Time-lapse seismic investigations commonly utilize conventional broadband seismic data, considered low-to-moderate resolution in our context. We present the first comprehensive time-lapse analysis of high-resolution seismic data by assessing the repeatability of P-Cable 3D seismic data (~30-350 Hz) with short offsets and high density of receivers. P-Cable 3D seismic datasets have for decades been used to investigate shallow fluid flow and gas hydrate systems. We analyze P-Cable HR4D seismic data from three different geological settings in the Arctic Circle. The first two are test sites with no evidence of shallow subsurface fluid flow, and the third is an active seepage site. Using these sites, we evaluate the reliability of the P-Cable 3D seismic technology as a time-lapse tool and establish a 4D acquisition and processing workflow. Weather, waves, tide, and acquisition-parameters such as residual shot noise are factors affecting seismic repeatability. We achieve reasonable quantitative repeatability measures in stratified marine sediments at two test locations. However, repeatability is limited in areas that have poor penetration of seismic energy through the seafloor such as glacial moraines or rough surface topography. 4D anomalies in the active seepage site are spatially restricted to areas of focused fluid flow and might likely indicate changes in fluid flow. This approach can thus, be applied to detect migration of fluids in active leakage structures, like gas chimneys.

INTRODUCTION

Seismic waves are sensitive to the amount and type of fluids, pore-pressure and geomechanical properties of the material they penetrate. When the physical properties in the subsurface vary in calendar time, they can be detected, monitored and modeled by repeating seismic datasets (Williamson et al., 2001, Ivanova et al., 2012, Nasser et al., 2016). For at least 20 years, time-lapse, or 4D seismic surveys, have been necessary for monitoring temperature, pore pressure and fluid saturation in production-related hydrocarbon reservoirs and at CO_2 storage sites (Landrø et al., 1999, Lumley, 2001, Chadwick et al., 2005, Johnston, 2013). Increasing demands for leakage control at onshore and subsea CO_2 storage sites, monitoring of near-surface seasonal changes, earthquakes or other types of geohazards (before and after) has furthermore caused an increase in the necessity of the method (Landrø and Amundsen, 2018).

The residual difference that is not related to physical property changes between a baseline survey (the first time-lapse survey acquired) and one or more seismic monitoring surveys (repeat surveys) affects the applicability of the time-lapse data and represents 4D seismic noise (Landrø, 1999, Vedanti and Sen, 2009). Positioning errors, varying tide and wave conditions, source and receiver variations, velocity change in the water column, or processing differences are typical sources of 4D noise (Nasser et al., 2016). Geologically complex areas are more prone to 4D noise than areas with confined sedimentary beds lacking tectonic lineaments, folds, sharp erosional surfaces, etc. (Malme et al., 2005, Misaghi et al., 2007, Nasser et al., 2016). Monitoring systems and processing workflows are designed for the specific purpose of 4D data to minimize this residual difference (Nasser et al. 2016).

The magnitude of real detectable changes in physical properties depends on the minimum size of subsurface features resolved with the 3D seismic technology utilized, as well as the initial elastic properties of the reservoir. Unlithified sedimentary packages are favorable 4D seismic targets because the elastic property response to fluid change is higher than that of harder, more consolidated rocks. Better detectability of 4D seismic anomalies and less 4D seismic noise improve the overall 4D quality.

To date, marine 4D seismic surveys are typically limited to conventional seismic frequencies (~5-120 Hz) well suited for monitoring deep reservoirs. Extending the 4D bandwidth towards higher frequencies combined with higher vertical and lateral resolution enable more accurate separation of smaller features (better 4D detection) which will increase the reservoir monitoring resolution in the shallower seismic interval (Lecerf et al., 2015). Calvert (2005) states that in future 4D technology, detection of smaller changes will become an increasing demand.

The high-resolution 3D (HR3D) P-Cable seismic system (~30-350 Hz) is conceived to produce data with a spatial resolution of 3-6 m, surpassing the resolution of conventional 3D seismic by one order of magnitude (Planke et al., 2009, Planke, 2013). For more than a decade, the P-Cable seismic system has been used to map shallow gas accumulations, gas hydrate systems and fluid flow structures such as gas chimneys (Petersen et al., 2008, Crutchley et al., 2010, Plaza-Faverola et al., 2011, Bünz et al., 2012). In recent years, several client- and multi-client P-Cable surveys have been acquired in the Barents Sea and Norwegian continental shelf, contributing to for example discovery of the Peon gas field (Eriksen et al., 2014). In a 4D sense, time-shifts and changes in acoustic impedance on P-Cable 3D seismic data can be assessed on an excellent resolution. It is, however, worth pointing out that the short streamer length (25-100 m) of the P-Cable seismic system limits seismic velocity and AVO analyses.

We investigate and discuss if and under what circumstances the high-resolution P-Cable seismic technology is applicable as a 4D seismic monitoring tool. To cover many different geological settings, weather conditions and the robustness of the acquisition procedure, we have acquired a baseline and repeated surveys in three areas in the Arctic (Figure 1). We describe the 4D acquisition, preprocessing, and 4D processing methods implemented on the three study sites; and present and evaluate schematic results of repeatability measures and seismic differences. All three sites offer different geological conditions whereby two of the sites (Lyngen and Snøhvit) are test-sites, where we do not expect any changes in the subsurface sediments (Hansen et al., 2011, Tasianas et al., 2016). The third site is the Vestnesa Ridge offshore Svalbard, a well-studied active fluid release and gas hydrate system in the Arctic. We discuss whether or to what extent 4D anomalies in the Vestnesa data can relate to natural subsurface changes and pore fluid dynamics.

STUDY AREAS

Test site 1: Lyngen area

The P-Cable datasets Lyngen 2012 and 2014 are acquired in the Lyngenfjord, a fjord in Northern Norway (Figure 1). The seafloor (380 to 440 ms Two-Way Traveltime (TWT) (~280-325m) is featureless and slightly dipping towards the margin of the fjord (Figure 2). The subsurface covered with the P-Cable data represents a post-glacial basin filled with mostly stratified sediments (unit 1) underlain by a distinct erosive contact reflecting a transition to moraine deposits (unit 2). Unit 1 is ~30 to 160 m thick (Figure 2). Within unit 2, two distinct

moraine ridges occur at about 60 m depth distance and appear as prominent, erosive and undulating horizons (Figure 2).

Test site 2: Snøhvit area

Two P-Cable datasets Snøhvit 2011 and 2013 are located in the Hammerfest basin area, 2 km south of the Snøhvit field in the western Barents Sea (Figure 1). Pockmarks and plough marks characterize an otherwise flat seafloor at ~440 to 470 ms TWT (~335-352 m) below sea surface (Figure 3). The seafloor pockmarks represent a record of previous fluid activity in the area; however, currently, there is no sign of any fluid release (Hansen et al., 2011, Tasianas et al., 2016). The 3D seismic data resolves the upper 225 m of the subsurface strata. The seismic can be divided into two main units separated by a distinctive, high amplitude unconformable horizon – the upper regional unconformity (URU) that absorbs most of the seismic energy (Figure 3). The upper unit consists of glacial-related sediments characterized by seismically chaotic, weaker amplitude reflectors of sub-horizontal to horizontal orientation. The lower unit comprises dipping reflection events between weaker-amplitude chaotic thin beds of early-middle Cenozoic age (Tasianas et al., 2016). This unit is interrupted by faults with small (<10 m) displacements. For the 4D analysis, we divide the subsurface into two depth intervals of similar thicknesses. Interval 1 is located between 440 and 590 ms TWT (covering mostly the glacial unit), and interval 2 is located between 590 and 740 ms TWT (covering most of the underlying dipping strata).

Vestnesa Ridge

Vestnesa Ridge is a large sediment drift with a ~5 km thick stratified sedimentary sequence located in 1200-1500 m water depth, extending from the western Svalbard continental slope towards the Molloy Ridge (Eiken and Hinz, 1993) (Figure 1). The site hosts an active fluid flow system with evidence of past and present-day gas seepage (Petersen et al., 2010, Bünz et al., 2012, Panieri et al., 2017, Sztybor and Rasmussen, 2017, Knies et al., 2018). We carried out the 4D seismic study (seafloor depth ~1230-1250 m) in an area of five large seafloor pockmarks (up to 700 m in diameter and 10 m deep) that area the seafloor expressions of underlying vertical fluid flow structures, so-called chimneys (Figure 4). Multi-year echo-sounder surveys detected active gas seepage from three of these pockmarks (termed Lomvi, Lunde and Torsk) (Smith et al., 2014, Panieri et al., 2017).

The seismic data show horizontal to sub-horizontal strata interrupted by focused sub-vertical fluid flow features (Figure 4). These chimneys show high variability in seismic signature with alternating blanked areas and high amplitude anomalies related to fluid perturbations and presence of gas hydrates/authigenic carbonates (Petersen et al., 2010, Panieri et al., 2017). The chimneys pierce through a high-amplitude reversed-polarity reflection ~1900 ms TWT interpreted as a gas-hydrate related bottom-simulating reflector (BSR) (Bünz et al., 2012) (Figure 4).

METHODS

Seismic Repeatability

Seismic repeatability relates to how accurate a survey is repeated in calendar time. Several 4D attribute measures can quantify repeatability (Kragh and Christie, 2002, Liu et al., 2009):

- *Time-shifts (TS)*: the time difference between two traces *a* and *b* where the squared difference in amplitude is minimum.
- *Cross-correlation (xcor/$\emptyset_{ab}$)*: is the cross correlation between traces a_i and b_i within time window t_1 –t_2
- *Predictability (PRED):* the percentage of the summed square cross-correlation within a time window divided by the summed product of the autocorrelations
- *Normalized root mean square (NRMS)*: the percentage normalized RMS difference of traces from two surveys

$$\emptyset_{ab} = \frac{\sum_{i=t-w/2}^{t+w/2} a_i b_i}{\sqrt{\sum_{i=t-w/2}^{t+w/2} a_i^2 \sum_{i=t-w/2}^{t+w/2} b_i^2}} \quad (1)$$

$$PRED = \frac{100 \times \sum \emptyset_{ab}(\tau) \times \emptyset_{ab}(\tau)}{\sum \emptyset_{aa}(\tau) \times \emptyset_{bb}(\tau)} \quad (2)$$

$$NRMS = 2\,\frac{RMS(Baseline - Monitor)}{RMS(Baseline) + RMS(Monitor)} \quad (3)$$

The RMS operator is defined as:

$$RMS(a_i) = \sqrt{\frac{1}{N}\sum_{i_1}^{i^2} (a_i)^2} \quad (4)$$

Where N is the number of samples a_t in the interval $t_1 - t_2$, and i_1 and i_2 represent time sample number for for t_1 and t_2

The cross-correlation and predictability measure range from 0-1 (or 0-100 %) and are sensitive to noise and changes in the earth's reflectivity, but insensitive to amplitude, static and phase changes (Kragh and Christie, 2002). Thus, if both traces anticorrelate, the predictability and cross-correlation is 1, or if the amplitude of the trace is half the amplitude of the other, it is still 1. NRMS is susceptible to all changes in the data and range between 0-2 (0-200 %). Random noise contributes to increasing this 4D measure. If both 4D surveys contain random noise, the measure is ~1.41. If they are phase-reversed compared to each other, the value will be ~2.

4D seismic acquisition

The P-Cable system (Figure 5) is a HR3D seismic acquisition system that can tow up to 18 short streamers (25-100 m) with short streamer spacing (6.25 to 12.5 m) resulting in dense CMP coverage with small bin sizes as low as 3.125 m (Planke et al., 2009, Petersen et al., 2010). The time-lapse datasets used in this study were acquired using 14 streamers of 25 m length and 12.5 m streamer spacing. Each streamer contains eight receivers with a group interval of 3.125 m.

All datasets are acquired using one mini-GI air gun with an injector/generator volume of 15/15 in^3 operated in harmonic mode with an air gun pressure of 160 bar (Lyngen and Snøhvit) and 170 bar (Vestnesa). The Lyngen 2012, Snøhvit (2011 and 2013) and Vestnesa 2012 surveys were operated with a 4-s shot interval, whereas Lyngen 2014 differs with a shot-interval of 3 s,

and Vestnesa 2013 with a shot-interval of 5 s (sail-line 1-4) and 6 s (sail-line 5-30). The difference in the shooting-interval for the Vestnesa 2013 data set is due to problems with air gun pressure supplied from the compressor.

For each of the sites, the planned acquisition lines and survey geometry of repeat surveys were identical to baseline surveys. GPS devices were located on the gun and both paravanes. The positioning of streamers was calculated through a catenary line equation, and the offset was updated using the direct arrival time for each trace (Crutchley et al., 2011). Towing depth, navigational control and weather conditions were assessed continuously. Despite that, potential deviations in the tracking system of the vessel and sea currents might affect the streamer array causing discrepancies of source-receiver geometry from survey to survey. Operational ship speed was typically 4 knots. An overview of the different survey parameters is listed in Table 1.

The two investigated P-Cable datasets from the Lyngen area (2012 and 2014) have an overlap of 3.3 km^2 (tab. 1). The weather conditions were less favorable in 2012, with 5-12 m/s recorded wind speed as opposed to 0-3 m/s during the acquisition in 2014. The datasets in the Snøhvit area (2011 and 2013) overlap by an area of 2.4 km^2. The weather and water temperature were comparable during both surveys with wind-speeds of 6-8 m/s in 2011 and 6-12 m/s in 2013. The datasets (2012 and 2013) from Vestnesa Ridge overlap by an area of ~ 10.7 km^2. The weather was slightly worse in 2012 with winds of 4-12 m/s compared to 1-7 m/s in 2013.

3D seismic processing

We conducted the 3D seismic processing sequence of the different datasets side-by-side using RadexPro software. The processing included removal of bad channels, geometry

assignment, tide corrections, compensation for amplitude loss (spherical divergence), band-pass filter, 3D binning at 6.25 x 6.25 m and NMO (Normal-Move out) correction, mean stack and 3D Stolt migration using a constant average water velocity (Table 2). Processing parameters for each dataset are listed in Table 1. Processes involving data-dependent operators were not applied.

Band-pass filter was chosen after inspection of the dominant frequency and frequency content of the different time-lapse datasets. The Lyngen 2012 and 2014 (25-35-300-400 Hz) showed comparable amplitude spectra with a common dominant frequency of 150 Hz (Figure 2). The Snøhvit time-lapse datasets showed a dominant frequency of 100 Hz with most spectral energy between 50 and 180 Hz (Figure 3). Consequently, we applied a relatively narrow frequency filter (50-70-150-180 Hz) for the 4D analysis. The Vestnesa 2012 and 2013 (30-50-275-350 Hz) showed comparable amplitude spectra with a dominant frequency of 175 Hz (Figure 4). Furthermore, we analyzed repeatability in three additional bandwidths of the Lyngen data: low-mid case (25-35-175-230 Hz), mid case (50-70-175-230 Hz), narrow case (50-70-140-180 Hz) to investigate the seismic repeatability for different frequency intervals.

Signal-to-noise ratios (S/N) of the different surveys (Table 4) was estimated as the ratio between the average RMS value of non-muted stack beneath the seafloor in a 100 ms time window and the same time-window of the water column. This is a practical way to estimate the signal-to-noise ratio, but not accurate, since the noise is measured in a window above the target zone. Due to signal decay with time, the S/N decreases with depth, as probably reflected in the differences between the Lyngen and Vestnesa S/N.

4D pre-processing

The preparation of the 4D seismic data included standard 4D pre-processing steps such as cutting seismic volume to a common coverage, creating common CMP numbers, CMP coordinates and inline and crossline numbers. In addition, we implemented pre-processing steps to reduce residual difference and improve repeatability between the datasets. Random, incoherent and coherent noise was suppressed in GeoTeric's post-stack noise cancellation algorithms (incl. a structurally oriented and edge-preserving finite impulse response median hybrid filter (SOFMH)) and a Tensor Diffusion algorithm (TDiffusion)). Furthermore, we applied a small bulk shift static correction and a phase reversal if necessary, and scaled amplitudes to a common average level (Table 2).

Seismic 4D processing

4D processing was carried out through five processing steps (Table 2) using a standard 4D calibration workflow in the software HRS Pro4D. We shortly describe the application of the different steps in Table 3. Guided by time (TS), cross-correlation (XC) thresholds and a correlation window, the workflow intends to correct for misalignments in phase, time, seismic amplitude and frequency between the base and monitor surveys. The thresholds were chosen after inspection of apparent time-shifts and cross-correlation values between the surveys. The correlation window was typically chosen globally, i.e., from the seafloor until reflections become too weak to indicate any geological features, or for the Vestnesa case, between seafloor (at ~1640 ms and 1840 ms TWT) and right above the BSR. This window is what we refer to as

"average". Otherwise, we chose a shallow correlation window (50-150 ms) when correcting for static changes (step 3).

There is a small spatially consistent time (depth) variant shift (<1ms) between the baseline and the monitor surveys in all case studies, which appears when comparing time-shifts of the upper and lower intervals (Figure 6, 8, 9). This consistent time variant shit can result from a slight NMO stretch due to an incorrect velocity model and use of the Stolt 3D migration that seems to induce some stretch. It is important to stress, however, that the stretch is minor, but due to the high-frequency content, significant to reduce seismic similarity and repeatability measures. Processing step 5 (time-variant-shift) is usually attributed to correct for velocity variations in the overburden. Under strict thresholds (time shift: 1 ms, cross-correlation: 90 %), we used this method to correct for the acquisition/processing related non-stationary time-shifts.

RESULTS

The 4D processing flow and step-wise results for the three case studies are presented in Figure 6 (Lyngen), Figure 8 (Snøhvit) and Figure 9 (Vestnesa). Each process improved repeatability measures (NRMS, time and phase shifts and cross-correlation) and reduced seismic differences (Table 2), with some exceptions. Step 4 (RMS scaling) did not show any effect for neither of the surveys and was therefore not applied.

After global adjustments (step 1 and 2), average time shifts between shallow and deeper intervals varied from 0.1-0.9 ms. Similarly, small time-shift variations (1-2 ms on average) were observed between inlines due to residual static differences (assumed to mainly be associated with

tide uncertainties). The trace-by-trace time corrections (step 3) resulted in a reduction of these residual time shifts in the shallower parts. Moreover, the final trace-by-trace time-variant shift process (step 5) efficiently improved the repeatability in the deeper intervals by reducing remaining small depth consistent time-differences (Figure 6, 8 and 9).

Repeatability of P-cable data in a fjord setting: Lyngen 2012 – 2014

3D seismic data from the Lyngen area were analyzed in the time window 400-650 ms. Here, the average NRMS value decreased from 0.94 to 0.47, and the average predictability increased from 0.77 to 0.81 at the end of the 4D processing flow (figure 6, step 1-5). Similarly, the phase and time-shifts decreased from 9.4 to 0.7 degrees and -0.7 to 0.01 ms respectively.

The Lyngen site consists of two main units:

Unit 1 (i.e., stratified sediments) has a final average NRMS value of 0.39, cross-correlation value of 0.88 and average time shift value of 0.006 ms (Figure 6, step 5). In places, this unit shows even better predictability and NRMS values of ~0.97 and ~0.28, respectively (Figure 6, step 5, sub-area 1). Remaining 4D anomalies of unit 1 appear as (1) striping imprint (Figure 6, step 5) due to small coverage gaps in 2014 and (2) cluster of 4D anomalies in the southern part above the peak of the moraine ridge (Figure 6, step 5).

Unit 2 has a more chaotic and undulating seismic facies caused by the moraine ridge and moraine material below (Figure 2). 4D processing resulted in a final NRMS value of 0.73 (Figure 6, step 5), a cross-correlation value of 0.73 (Figure 6, step 5) and an average time-shift difference of 0.004 ms (Figure 6, step 5). Repeatability decreases with depth within this unit (Figure 6, step 5).

We analyzed the repeatability of the Lyngen data using different frequency bandwidths (Figure 7 A). Interestingly, the repeatability prior to 4D processing increased by simply decreasing the frequency bandwidth (i.e., 0.94 for broad and 0.73 for narrow frequency band). After processing, the NRMS value for Unit 1 and 2 using the broad frequency band was 0.35 and 0.79 respectively (Figure 7 B). The mid-case scenario (where we reduce the frequency band around the dominant frequency) produced the lowest average NRMS of 0.23 (unit 1) and 0.70 (unit 2) (Figure 7 B). The narrow-case (cutting more high frequencies) did not result in further increase of repeatability but resulted in an average NRMS to 0.30 for unit 1 (Figure 7 B). A decrease in signal-to-noise ratio when moving the frequency band below the dominant frequency might explain this phenomenon (Figure 7 C).

Repeatability of P-Cable data in a formerly glaciated margin: Snøhvit 2011 – 2013

During the 4D processing, the average NRMS and predictability (time-window 440-740 ms TWT) improved from 0.62 to 0.36 and 0.83 to 0.89, respectively (Figure 8, step 1-5). Similarly, the globally derived phase and time shifts are adjusted from 1.3 to -0.5 degrees and 0.5 to -0.03 ms, respectively. Moreover, the two depth-intervals became comparable in 4D quality (Figure 8, step 5).

Between the baseline and the final processed monitor survey, the underlying dipping reflectors are close to perfectly matched while some patches of 4D anomalies still exist especially along the Seafloor and URU (Figure 8, step 5). Other remaining 4D anomalies are as comparable to the Lyngen data, weak inline-directed amplitude differences. To investigate if the random 4D anomalies were related to faults, plough-marks (Osdal et al., 2010) or buried pockmarks, we calculated variance of the Snøhvit 2011 seismic for both interval 1 and 2.

Variance evaluates the continuity of seismic reflections and is an ideal attribute for identifying faults and fractures. Areas with very low coherence (marked as blackened areas in Figure 8, step 5) are draped on top of the predictability maps and indicate the occurrence of faults. These low-variance areas coincide with the 4D anomalies (low predictability areas). Along the seafloor, the location of pockmarks (Figure 3) coincide with the 4D anomalies (Figure 8, step 5) and subsurface faults.

Repeatability of P-cable data in a deep-water Arctic basin: Vestnesa 2012-2013

The pre-processed seismic difference between Vestnesa 2013 and 2012 in time window 1640-1840 ms shows pre-processed NRMS and predictability values of 0.71 and 0.77, respectively (Figure 9, Initial). Here, inline-striping imprints caused prominent time-shift anomalies between the datasets, and we observed significant 4D amplitude anomalies at chimney locations. The overall 4D process improved the average NRMS and predictability to 0.38 and 0.86, respectively (Figure 9, Initial to 5). The final 4D anomalies between Vestnesa 2012 and 2013 are mostly concentrated in seismic chimneys and along the faults where 4D changes caused by fluid flow are expected (Figure 9). The best seismic repeatability was found in the strata outside the chimneys, presenting an average NRMS and predictability of 0.3 and 0.95, respectively (Step 5, Figure 9).

DISCUSSION

4D noise connected to P-Cable acquisition

The main acquisition-related factors influencing the signal-to-noise ratio and reproducibility of marine-towed seismic data typically relate to the acquisition system and execution of the survey; such as survey geometry and operating parameters, or it relates to environmental effects (Calvert, 2005).

Acquisition system and execution of the surveys

On the final Lyngen difference data, slightly poorer repeatability relate to some data-coverage gaps (Figure 9, step 5). Besides that, we do not identify any significant differences, which relate to survey geometry or execution at any of the sites. A reasonable reproducibility of survey geometry, source signal, and noise level is thus manifested in the similarity in amplitude spectra (Figure 2-4) between the baseline and monitor surveys at all locations. By using the same vessel to acquire the different surveys, the ship-noise effect on repeatability was also minimized. The compactness of typical high-resolution seismic systems led to less drift and feathering than conventional towed marine streamers. The typical dense grid of the data reduces positioning errors by decreasing the lateral positioning shifts between the baseline and monitor survey to a couple of meters (within the bin-size of the surveys).

Weather and water effects

Environmental effects are typically associated with weather and water-effects (Calvert, 2005). To minimize weather effects, we collected all datasets at the same time of the year and in similar wave conditions < 2 m. Moreover, the different time-lapse datasets were processed using identical water-velocity and tide-corrected. However, the average water velocity or water column height probably differed somewhat from year to year causing the minor global time-shift

differences (1-2 ms) between the surveys (Table 4). As an example, the average time shift difference of 1 ms at the seafloor of the Vestnesa 4D datasets corresponded to a small, ~ 1 m/s average velocity change between the surveys. Furthermore, both Lyngen and Snøhvit datasets, as well as Vestnesa 2013 have significant noise in inline direction manifested in small inline tide-periodical shifts. Vestnesa 2013 was in contrast smooth, without visible inline striping trends.

The slight changes in water column height or velocity might be related to changes in temperature, salinity or local water column height differences. The weather was worse during acquisition of Lyngen 2012, Snøhvit 2013 and Vestnesa 2012 compared to their time-lapse pair indicated by ~ 4-10 m/s increase in average wind-speed (Table 4). This effect is possibly evident in Lyngen 2012 and Snøhvit 2013 as low-frequency noise, and in Lyngen 2012 and Vestnesa 2012 as stronger static variations (compared to Lyngen 2014 and Vestnesa 2013, respectively) (Figure 2 and 4) due to rougher sea, swells or more frequent changes in water properties. The weather effect is also evident from the signal-to-noise ratio between the surveys, i.e., the Vestnesa data has a lower signal to noise ratio in 2012 (12.9) compared to in 2013 (18.9). Conversely, the Lyngen 2014 and Snøhvit 2011 are acquired in better weather yet show lower S/N compared to their time-lapse match. A more moderate S/N can alternatively be explained by other dominant noise-related factors such as trace-fold (i.e., a measurement of the average geographical distance between each trace) or shot generated noise.

We reflected on the possibility that the gas bubbles from the Vestnesa seepage site could have an additional effect on water column velocities. However, being a relatively low flux seepage site (Panieri et al., 2017), we did not expect it to have any visible effect, which our analysis confirmed. That is, we could not identify any differences in residual time-shifts in areas of active- or inactive seep sites. Overall, the final time shifts (after tide corrections, bulk shift,

statics and time variant shift using 1 ms threshold) along seafloor are as low as -0.2 to 0.2 ms here, which is to the sample rate (0.25 ms).

Trace fold and repeatability

A higher trace-fold normally lead to a better signal-to-noise ratio. Andorsen and Landro (2000) show that the RMS difference between time-lapse data decreases linearly from approximately 16 % to 3-4 % between unstacked and 50 trace-fold data. Snøhvit 2011 data have a trace fold of 7 and S/N of 31.5 whereas Snøhvit 2013 data have a trace-fold of 11.5 and an S/N of 43, which might be explained by a comparable relationship between trace-fold and noise level.

The Vestnesa 4D datasets are possibly affected by the difference in the shooting rate (Table 1), due to the combined effect on trace-fold and residual shot noise. The different shot-rate (4 s: Vestnesa 2012 and 5-6 s: Vestnesa 2013) likely cause the variation in average trace-fold, which is 7.2 for Vestnesa 2013 compared to 8.7 for Vestnesa 2012. To investigate the isolated effect of average trace-fold and total S/N, we re-binned the Vestnesa 2013 data to half the bin-size (3.125) and compared the two identical volumes of different bin-size. We found that the larger shot-interval that reduced the trace-fold of the Vestnesa 2012 survey may have contributed to a ~20 % reduction in ambient noise (related to lower trace-fold), but only a ~10 % reduction in overall noise that is considered to be a combination of ambient noise and residual shot noise (see appendix B for calculations). However, it is not a direct positive relationship between trace-fold and increased signal-to-noise ratio, since Vestnesa 2012 has a S/N of 12.9 and Vestnesa 2013 a S/N of 18.9. Thus, other noise-effects between the datasets must explain the difference in noise level.

Residual shot noise

Energy arriving at the receivers from previous shots may introduce an additional source of noise affecting data repeatability. A larger time interval between firing shots not only reduce the average trace-fold but can contribute positively to less noise interference from previous shots. The non-repeatable nature of residual shot noise can typically cause poorer repeatability of time-lapse data (Landrø, 2008).

Due to relatively shallow water in the Lyngen area, we found that the seafloor reflection-multiples bounce ~7 times between two shots at a shot-rate of 3 s (3 s/0.4 s TWT to seafloor). Every time this occurs, more energy will be attenuated. Consequently, the sound energy from the previous shot is greatly attenuated, hence, therefore likely insignificant whether fired at 3 or 4s.

The Vestnesa data has on contrary approximately four times greater water-depth than the Snøhvit and Lyngen data (Table 4, B-1) and will thus be more affected by residual shot noise. Compared to Vestnesa 2013, more residual shot noise is expected in Vestnesa 2012 since the survey is acquired with a shorter shot-interval. Inspecting the reflective energy difference in the water-column confirms this assumption (Figure 10).

Landrø (2008) investigated the effect of shot generated noise by analyzing and modeling amplitude decay versus recording time for conventional marine streamers. Using their proposed equation from that study (see appendix B), we find that the reduction in shot interval between the Vestnesa 2012 and 2013 surveys can cause a decrease in residual shot noise by ~77 %, however, consequently an increase in ambient noise by ~20 % due to less average fold. The residual shot noise is indicated to represent around ~ 53 % of the total noise in the Vestnesa 2012 survey (and 16 % of the total in Vestnesa 2013). Assuming this is true, the remaining ambient noise

difference is likely related to weather and wave effects and is calculated to cause a ~ 38 % difference in noise level between the surveys. We conclude that the difference in signal-to-noise ratio between the surveys is likely a combination of residual shot noise, weather and water-effects, and trace-fold.

Noise in the Snøhvit data

There is, however, an overall noticeable difference between the three sites that do not seem to be explained by weather, fold or residual shot noise. That is the apparent higher level of 3D and 4D noise in the Snøhvit data relative to the two other sites, and the significant difference in signal-to-noise between the Snøhvit surveys (31 in 2013 versus 43 in 2011). We speculate whether some of this noise is related to production at the Snøhvit field. The survey, in fact, covers the main hub at the seafloor (Hansen et al., 2011).

The high frequencies emitted by the source are quickly reflected at the Snøhvit site due to a relative hard seafloor and higher-velocity strata, reflected in a low dominant frequency. Lack of high frequencies might, therefore, justify the action of applying a relatively narrow frequency filter compared to the other surveys to reduce 3D and 4D noise here.

Processing effects on P-Cable repeatability

The pre-processing steps significantly increased the repeatability (Table 2). Remaining time-related static differences and seismic velocity changes were further adjusted for during the local time-shift correction routines. In particular, the 4D processing routine of all case studies showed that the second trace-by trace time correction was necessary for improving repeatability

by correcting for smaller residual static changes. Applying pre-stack residual static corrections based on a time average calculated along the seafloor could lead to a better final repeatability. However, this processing step could compromise the resolution of the data by smoothing the shape and depth of a small pockmark or plough-marks.

Match of phase and amplitude, as well as rescaling the amplitudes in step 4 provided negligible improvements.

Geology related time-lapse seismic differences

From the three investigated sites, we achieved a good sense of the effect that major geological structures have on the repeatability of the time-lapse data. We particularly observed lower repeatability associated with harder or more undulating morphology, such as the moraine ridges in Lyngen and along URU in the Snøhvit area (Table 4). Slight deviations in source-receiver positions and orientations across complex surfaces cause differences in seismic scattering signals (Misaghi et al., 2007). In turn, this probably led to some discrepancies in collapse of diffraction hyperbolic events during migration and distortion of traces in form on small time-shifts or amplitude variations beneath (Malme et al., 2005, Osdal et al., 2010). The seismic response from the lowermost moraine ridge in the Lyngen area is dominated by diffractions (Figure 11). However, there are places where no 4D anomalies are observed indicating that the primary reflections are undisturbed (Figure 2, 3, 4). Only (monitor) amplitudes of 80-100 % similarity to the reference within a sliding time-interval of 1 ms were adjusted during the last time-variant 4D processing step. This implies that we are able to repeat

most amplitude reflections along the unconformities and undulating surfaces using rather strict thresholds (e.g., Figure 11).

The subsurface fluid flow system of the Vestnesa ridge is incised in soft marine sediments where we obtained an average NRMS value of 30 % and predictability of 95 % (Figure 8). Within gas chimneys, the repeatability is lower and the validity of 4D anomalies are less reliable. Scattered energy and distortion of signals can as mentioned lead to locally poorer repeatability. In contrast to anthropogenic controlled production of reservoirs, it is more challenging to predict or model subsurface changes at natural seep sites. However, we expect more 4D anomalies associated with pore-fill changes (saturation or pressure changes) underneath the actively leaking pockmarks (Figure 12). In the shallow subsurface (0-50 ms) of the active pockmarks, we do observe a higher abundance of 4D anomalies compared to just underneath the inactive pockmarks (Fig. 12). We hypothesize that at least parts of this intensification of 4D anomalies (i.e., within chimneys and in the shallow subsurface of active pockmarks) are an effect of active fluid flow through the chimneys (Figure 9, step 5).

As a control on the 4D anomalies, we tested the repeatability of small structures within and outside of the chimney area. By comparing (manual) interpretation of small-scale faults on Vestnesa 2012 and 2013, we show that complex chimney structures in marine contourite deposits can be repeated, at least locally (Figure 13). The figure also shows that 4D anomalies occur in intervals along the chimneys restricted to areas around fractures and faults, especially at their termination. Such observations suggest that time-lapse investigations of these chimney features are potentially suitable for constraining fluid migration through faults and fractures.

Repeatability of P-Cable data compared to conventional seismic

The highest repeatability values were achieved for the undisturbed well-stratified region on the Vestnesa Ridge (i.e., average NRMS of 30%). The stratified unit at the Lyngen region (i.e., unit 1) has average NRMS values that range from 28-39%. The lower unit characterized by chaotic facies, shows poor repeatability (i.e., average NRMS of 73%). Repeatability of the Snøvit data sets is comparable to that of the Lyngen data (i.e., 36%).

Among low (to-mid) frequency bandwidth data (the common bandwidth of industrial time-lapse data), the average NRMS achieved for marine-streamer 4D seismic data today is 20-30 % (Landrø and Amundsen, 2018). Landrø and Amundsen (2018) state that achieving an NRMS below 20 % between repeats of marine-streamer data would largely depend on excellent weather, wave and water-column conditions.

NRMS generally increases with higher frequency content for the same amount of time or positioning shifts (4D noise) (Landrø et al., 1999, Kragh and Christie, 2002, Eiken, 2005, Lecerf et al., 2015). As an example, Lecerf et al. (2015) calculated an NRMS value of 18.6 and 27.4 for fixed small time-shifts at 38 and 53 Hz, respectively. That is a 10 % decrease in NRMS for the same time-shift by only decreasing the frequency by 20 Hz. In a repeatability study of 50-150 Hz VSP (Vertical Seismic Profile) data, Pevzner et al. (2011) show pre-stack NRMS of 20-30 % of the CO2CRC Otway Project Case Study. In another study using a narrow, low frequency bandwidth of 5-40 Hz, Anderson and Landrø (2000) show examples of zero-offset VSP data (10-fold stack) with a very low NRMS-error, 2-4 %. Hatchell et al. (2017) tested the repeatability of the HR3D P-Cable data by comparing a line from a 3D survey with a 2D repeat. In a similar geological setting as the stratified unit of Lyngen, they achieved an NRMS as low as 15 %.

In this study, we achieved comparable NRMS measures between the lower frequency and noisier Snøhvit data and the higher-frequency and cleaner Lyngen data. Disregarding the frequency content, time-lapse data with varying residual noise levels might appear of similar 4D quality. Narrowing the bandwidth around the dominant frequency (Lyngen, mid-low case; NRMS 23 %) where the S/N should be at highest, might be an effective way to indicate a typical top-end repeatability (~23 %) and assess the amount of non-repeatable sources. Considering this, the main difference in comparison to our results (~30-40 %) and Hatchell et al., (2017) NRMS measures (15 %), is that they used 100 m long streamers, a 10 times larger source and repeated the line in the same period. Repeating the line within just a couple of hours to days as well as the long streamers and source should be ideal for testing the lower end of the NRMS for that type of acquisition-setup and frequency range. All these effects in addition to a higher average fold are beneficial for producing higher repeatability, which likely clarifies why Hatchell et al., (2017) NRMS results are better.

Considering a higher dominant frequency and finer resolution than typical historical time-lapse data, we expected somewhat higher NRMS measures than the average NRMS for conventional 4D data today. It is worth stressing that the seismic resolution presented here is about 4 times higher than conventional broadband 3D seismic data. Depending on target, however, if a somewhat lower resolution were acceptable, one would also increase the repeatability somewhat by increasing the CMP bin-size and therefore trace-fold, as this will enhance the signal-to-noise ratio, leading to less residual differences. A higher signal-to-noise ratio can also be obtained without compromising the resolution by acquiring data with shorter sail-line spacing. Conversely, a less percentage of data overlap should lead to lesser S/N and thus poorer repeatability. This effect is illustrated by Landrø (1999) who shows how the RMS

difference increases with shot-separation. Nevertheless, we conclude that a repeatability of 30-40 % is acceptable, which should be promising for future 4D high-resolution investigations.

We suggest a few acquisition- and processing related factors worth considering prior to potential future comparable time-lapse studies; such as implementing a wave-gauge to measure water-level, 4D binning and calculations to more accurate streamer positioning (for more details, see appendix C).

CONCLUSIONS

High-resolution 3D seismic datasets provide a detailed and accurate image of the shallow subsurface typically down to 500-1000 m below the seafloor. We propose a processing workflow and demonstrate that the small-offset high-resolution P-Cable 3D seismic system (~30-350 Hz) can be used as a time-lapse tool resolving changes in acoustic impedance on a meter scale (~3-6 m). We find that the seismic repeatability is strongly geology-dependent. In stratified marine sediments, we find NRMS (Normalized RMS error) measures comparable to today's 4D seismic NRMS average (NRMS ~ 30 %). In glacial sediments and harder sedimentary rocks we estimate an NRMS of 30-40 %, and in more complex moraine material, the NRMS-level is 70-75 %. Important factors that influence the repeatability are accurate repetition of acquisition setup, calm weather and minimal wave activity as well as sufficient time between each shot (i.e., to minimize noise from previous shot). At the active fluid flow and gas hydrate system of the Vestnesa Ridge, we obtain high NRMS in gas chimneys and low NRMS outside gas chimneys. Moreover, we observe high NRMS in the shallow subsurface below active pockmarks (bubbles rising from seafloor and elevated methane concentrations) and low NRMS in the shallow part

beneath passive pockmarks (no bubbles observed, lower methane concentrations). We suggest that these observations indicate detection of real 4D anomalies related to fluid flow, which we find promising for potential future 4D investigations of fine-scaled geology and fluid-related differences. The ability to resolve fluid related changes on a very fine scale may open up new vistas for industrially and academically oriented gas hydrate and fluid flow communities.¨

ACKNOWLEDGMENTS

The project is funded by VISTA – a basic research program in collaboration between The Norwegian Academy of Science and Letters, and Statoil. The research is also a part of the Centre for Arctic Gas Hydrate, Environment, and Climate and was supported by the Research Council of Norway through its Centres of Excellence funding scheme grant No. 223259. We further thank the crew and scientists onboard RV Helmer Hanssen for assistance in acquiring the seismic data on the various cruises, and DECO Geophysical, CGG HampsonRussell, GeoTeric and Schlumberger for software and support. We thank Ed Kragh and two other anonymous reviewers for constructive comments and ideas to improve the manuscript.

APPENDIX A
F-K SPECTRUM TO INVESTIGATE FREQUENCY AND REFLECTOR DEPENDENT 4D NOISE

Plotting seismic difference in an F-K spectrum is another way to investigate potential relation of seismic frequency and dip of reflections on repeatability (Eiken et al., 2003). Such

analysis is however insensitive to 4D amplitude strength. To account for that, one might regard the lowest percentage (10 %) of the amplitudes as background noise and remove these amplitudes before the analysis. The F-K Spectrum of the seismic difference between Lyngen 2014 and 2012 indicates that 4D noise tends to be scattered in frequencies ranging between 100-200 Hz in sub-horizontal reflector-dip orientations compared to the original spectrum that was vertically centered on flat events (Figure A-1).

APPENDIX B

RESIDUAL SHOT NOISE CALCULATIONS

To better understand the apparent noise in the data, we calculated how much it is possible to improve the S/N ratio and thus the 4D quality by reducing the shot rate from 4 to 5 s by using the equation in Landrø (2008):

$$\frac{S}{N} = \frac{S}{s(t)+n(t)} = \frac{\frac{P_1 e^{-\pi f t \div Q}}{t^2} + \frac{P_2}{t} R_0{}^{\alpha t}}{\frac{P_1 e^{-\pi f (t+\tau) \div Q}}{(t+\tau)^2} + \frac{P_2}{(t+\tau)} R_0{}^{\alpha (t+\tau)} + n(t)} \qquad \text{(B-1)}$$

If the noise apparent in the data consists of shot-induced noise (*s)* and ambient noise (*n)* at a given recording time t and a shot interval τ the signal-to-noise ratio (S/N) can be calculated from this formula (Landrø, 2008).

P_1 and P_2 are scalars related to source strength and water level. We used 20 000 and 100, respectively, which is same values as used in Landrø (2008) (we observe that changing these values does not change the results much). R_0 is the dominant reflection coefficient of the seafloor (usually 0.3 to 0.4, we used 0.3 due to relatively soft sediments), Q is a constant of 80 that represent exponential decay (of energy), α is a fitting parameter representing the number of

multiple reflections, we used 0.5 (experimental value). Finally, f should represent a typical frequency in the data; we used 175 Hz.

From this equation, we calculated a common signal value of 21.19 at 1700 ms TWT depth. At a shot-interval of 4 s, we calculated a shot induced noise value s(4) = 0.57. The corresponding shot induced S/N becomes (21.19/0.567 =) 37.3. Exchanging the shot-interval of 4 s in the formula with 5 and 6 s give a new shot induce noise value of (s(5)=) 0.264 and (s(6)=) 0.126, respectively. Thus, a 1-s increase in shot-interval from 4 to 5 s cause a 53 % decrease in shot induced noise, and a 2 s increase, from 4 to 6 s, cause a continued decrease of shot induced noise by 77 %. Since most lines where acquired with a 6-s shot interval (average is 5.9), we extend the calculations by assuming that the survey was shot with 6-s shot interval.

Assuming further that the rest of the noise apparent in the data is ambient noise n(t) (e.g., caused by weather) and by use of the true calculated S/N ratio of Vestnesa 2012 and 2013 we infer the ambient noise n(t) in the

Vestnesa 2012 to be:

$$\frac{S}{N} = \frac{S}{s(t)+n(t)} = \frac{S}{x} \rightarrow 12.9 = \frac{21.9}{x} \rightarrow x = 1.64 \rightarrow n(t) = 1.64 - 0.567 = 1.076$$

And, in Vestnesa 2013 to be:

$$\frac{S}{N} = \frac{S}{s(t)+n(t)} = \frac{S}{x} \rightarrow 18.7 = \frac{21.9}{x} \rightarrow x = 0.882 \rightarrow n(t) = 0.882 - 0.126 = 0.756$$

When shooting with longer time-interval, at the same sailing speed the trace fold (traces in each bin) will be reduced linearly if the average sailing steep remains constant between the surveys. In theory, the increase of the shot-rate from 4 to 6 s causes the true fold of 8.7 in 2012 to be reduced to 5.8 (and from 4 to 5 s to be reduced to 7.2, which is the actual trace-fold of Vestnesa 2013). The data binned with 3.125 m got a new average trace-fold of 2.75, and we

further calculated a new average S/N of 15.9. Assuming a linear relationship between the fold and ambient noise, we find this relationship between noise and average fold for Vestnesa 2013:

$$n(t) = -0{,}1146 * FOLD + 1{,}4832 \qquad \text{(B-2)}$$

For the Vestnesa 2012 with a fold of 8.7 we achieve an ambient noise value of 0.49, and for the Vestnesa 2013 with a fold of 7.2, the ambient noise value is 0.62. This represents a 0.134 difference in ambient noise level, which might be fold related.

APPENDIX C

LESSONS LEARNED AND SUGGESTIONS TO IMPROVE HR4D DATA

We consider a few acquisition- and processing related factors worth considering prior to potential future comparable time-lapse studies.

A wave-gauge could be installed to better correct for static differences between the baseline and repeat(s) related to water level and tide-differences, and one should consider calculating individual measures by preferable several CTD stations at the site prior to the acquisition. Furthermore, it is important to be aware of shot induce noise in deep waters and how to minimize it (large enough shot interval).

We used a catenary line to calculate the geographical position of each streamer. However, due to i.e., surface currents, the cross-cable and streamer are not always following a perfect catenary line. Thus, using a polygon fitted line equation can lead to a more accurate positioning of the data (Crutchley et al., 2011). Not considered in this study 4D binning is moreover a process that should lead to better repeatability. Finally, a more advanced and accurate velocity

model than used in this study can add in a better migration process (for example Kirchhoff migration) and thus should in theory lead to better collapse of diffractions.

REFERENCES

Andorsen, K., and M. Landro. 2000, Source signature variations versus repeatability-a study based on a zero-offset VSP experiment. Journal of Seismic Exploration, **9**, no. 1,61-72.

Bünz, S., S. Polyanov, S. Vadakkepuliyambatta, C. Consolaro, and J. Mienert. 2012, Active gas venting through hydrate-bearing sediments on the Vestnesa Ridge, offshore W-Svalbard. Marine Geology, **332**,189-197.

Calvert, R. 2005, Insights and methods for 4D reservoir monitoring and characterization: Society of Exploration Geophysicists and European Association of Geoscientists and Engineers.

Chadwick, R., R. Arts, and O. Eiken. 2005, 4D seismic quantification of a growing CO2 plume at Sleipner, North Sea. Paper read at Geological Society, London, Petroleum Geology Conference series.

Crutchley, G. J., C. Berndt, D. Klaeschen, and D. G. Masson. 2011, Insights into active deformation in the Gulf of Cadiz from new 3-D seismic and high-resolution bathymetry data. Geochemistry, Geophysics, Geosystems, **12**, no. 7. doi: doi:10.1029/2011GC003576.

Crutchley, G. J., I. A. Pecher, A. R. Gorman, S. A. Henrys, and J. Greinert. 2010, Seismic imaging of gas conduits beneath seafloor seep sites in a shallow marine gas hydrate province, Hikurangi Margin, New Zealand. Marine Geology, **272**, no. 1–4,114-126. doi: https://doi.org/10.1016/j.margeo.2009.03.007.

Eiken, O. 2005, Repeatability issues of time-lapse marine seismic data. Paper read at 9th International Congress of the Brazilian Geophysical Society & EXPOGEF, Salvador, Bahia, Brazil, 11-14 September 2005.

Eiken, O., G. U. Haugen, M. Schonewille, and A. Duijndam. 2003, A proven method for acquiring highly repeatable towed streamer seismic data. Geophysics, **68**, no. 4,1303-1309.

Eiken, O., and K. Hinz. 1993, Contourites in the Fram Strait. Sedimentary Geology, **82**, no. 1-4,15-32.

Eriksen, F. N., M. Assad, O. K. Eriksen, H. H. Stokke, and S. Planke. 2014, HiRes P-Cable 3D Data for Shallow Reservoir Mapping and Geohazard Predictions–Case Examples from the Barents Sea. Paper read at Near Surface Geoscience 2014-First Applied Shallow Marine Geophysics Conference.

Hansen, O., O. Eiken, S. Østmo, R. I. Johansen, and A. Smith. 2011, Monitoring CO2 injection into a fluvial brine-filled sandstone formation at the Snøhvit field, Barents Sea, SEG Technical Program Expanded Abstracts 2011: Society of Exploration Geophysicists. 4092-4096.

Hatchell, P., R. Kamarudin, J. Lopez, S. Bakku, Z. Yang, K. Wang, V. Gee, J. Mestayer, K. King, and A. Kudarova. 2017, Low-cost high-resolution 3D and 4D seismic for deepwater fields. Paper read at 2017 SEG International Exposition and Annual Meeting.

Ivanova, A., A. Kashubin, N. Juhojuntti, J. Kummerow, J. Henninges, C. Juhlin, S. Lüth, and M. Ivandic. 2012, Monitoring and volumetric estimation of injected CO2 using 4D

seismic, petrophysical data, core measurements and well logging: a case study at Ketzin, Germany. Geophysical Prospecting, **60**, no. 5,957-973.

Johnston, D. H. 2013, Practical applications of time-lapse seismic data: Society of Exploration Geophysicists.

Knies, J., M. Daszinnies, A. Plaza-Faverola, S. Chand, Ø. Sylta, S. Bünz, J. E. Johnson, R. Mattingsdal, and J. Mienert. 2018, Modelling persistent methane seepage offshore western Svalbard since early Pleistocene. Marine and Petroleum Geology, **91**,800-811.

Kragh, E., and P. Christie. 2002, Seismic repeatability, normalized rms, and predictability. The Leading Edge, **21**, no. 7,640-647.

Landrø, M. 1999, Repeatability issues of 3-D VSP data. Geophysics, **64**, no. 6,1673-1679.

Landrø, M. 2008, The effect of noise generated by previous shots on seismic reflection data. Geophysics, **73**, no. 3,Q9-Q17.

Landrø, M., and L. Amundsen. 2018, Introduction to Exploration Geophysics with Recent Advances. www.bivrostgeo.no.

Landrø, M., O. A. Solheim, E. Hilde, B. O. Ekren, and L. K. Strønen. 1999, The Gullfaks 4D seismic study. Petroleum Geoscience, **5**, no. 3,213-226.

Lecerf, D., J. Burren, E. Hodges, and C. Barros. 2015, Repeatability measure for broadband 4D seismic, SEG Technical Program Expanded Abstracts 2015: Society of Exploration Geophysicists. 5483-5487.

Liu, G., S. Fomel, L. Jin, and X. Chen. 2009, Stacking seismic data using local correlation. Geophysics, **74**, no. 3,V43-V48.

Lumley, D. E. 2001, Time-lapse seismic reservoir monitoring. Geophysics, **66**, no. 1,50-53.

Malme, T. N., M. Landrø, and R. Mittet. 2005, Overburden distortions—Implications for seismic AVO analysis and time-lapse seismic. Journal of Geophysics and Engineering, **2**, no. 2,81.

Misaghi, A., M. Landrø, and S. A. Petersen. 2007, Overburden complexity and repeatability of seismic data: Impacts of positioning errors at the Oseberg field, North Sea. Geophysical prospecting, **55**, no. 3,365-379.

Nasser, M., S. Ronen, and J. Stammeijer. 2016, Introduction to this special section: 4D seismic. The Leading Edge, **35**, no. 10,828-830. doi: 10.1190/tle35100828.1.

Osdal, B., S. Grude, and M. Landrø. 2010, Sea bed diffraction and impact on 4D seismic data–observations from synthetic modelling and field data. Paper read at 72nd EAGE Conference and Exhibition incorporating SPE EUROPEC 2010.

Panieri, G., S. Bünz, D. J. Fornari, J. Escartin, P. Serov, P. Jansson, M. E. Torres, J. E. Johnson, W. Hong, and S. Sauer. 2017, An integrated view of the methane system in the pockmarks at Vestnesa Ridge, 79° N. Marine Geology, **390**,282-300.

Petersen, C., S. Bunz, S. Hustoft, and J. Mienert. 2008, 3D seismic imaging of marine gas hydrates in Arctic sediments of the Vestnesa Ridge off the W-Svalbard margin. Paper read at Proc 6th Int Conf Gas Hydrates (ICGH 2008).

Petersen, C. J., S. Bünz, S. Hustoft, J. Mienert, and D. Klaeschen. 2010, High-resolution P-Cable 3D seismic imaging of gas chimney structures in gas hydrated sediments of an Arctic sediment drift. Marine and Petroleum Geology, **27**, no. 9,1981-1994.

Pevzner, R., V. Shulakova, A. Kepic, and M. Urosevic. 2011, Repeatability analysis of land time-lapse seismic data: CO2CRC Otway pilot project case study. Geophysical prospecting, **59**, no. 1,66-77.

Planke, S. 2013, P-Cable High-Resolution 3D Seismic Imaging of Gas Hydrates and Shallow Gas. Paper read at 75th EAGE Conference & Exhibition-Workshops.

Planke, S., F. N. Eriksen, C. Berndt, J. Mienert, and D. Masson. 2009, P-Cable high-resolution seismic. Oceanography, **22**, no. 1,85.

Plaza-Faverola, A., S. Bünz, and J. Mienert. 2011, Repeated fluid expulsion through sub-seabed chimneys offshore Norway in response to glacial cycles. Earth and Planetary Science Letters, **305**, no. 3–4,297-308. doi: 10.1016/j.epsl.2011.03.001.

Smith, A. J., J. Mienert, S. Bünz, and J. Greinert. 2014, Thermogenic methane injection via bubble transport into the upper Arctic Ocean from the hydrate-charged Vestnesa Ridge, Svalbard. Geochemistry, Geophysics, Geosystems, **15**, no. 5,1945-1959.

Sztybor, K., and T. L. Rasmussen. 2017, Diagenetic disturbances of marine sedimentary records from methane-influenced environments in the Fram Strait as indications of variation in seep intensity during the last 35 000 years. Boreas, **46**, no. 2,212-228.

Tasianas, A., I. Martens, S. Bünz, and J. Mienert. 2016, Mechanisms initiating fluid migration at Snøhvit and Albatross fields, Barents Sea. arktos, **2**, no. 1,26.

Vedanti, N., and M. K. Sen. 2009, Seismic inversion tracks in situ combustion: A case study from Balol oil field, India. Geophysics.

Williamson, J., R. Chadwick, W. Rowley, and O. Eiken. 2001, Saline aquifer CO2 storage: a demonstration project at the Sleipner Field: Work Area 5 (Geophysics): gravity modelling of the CO2 bubble.

LIST OF FIGURES

Figure 1. Overview map, showing the location of the different P-Cable seismic 4D survey sites, the Lyngen area, the Snøhvit area and the Vestnesa ridge.

Figure 2. Seismic bathymetry (indicating seismic coverage) and inline example of the Lyngen 2012 and 2014 data. A: Lyngen 2012 (baseline) and B: Lyngen 2014 (monitor). C: Amplitude spectra of the two datasets. The main geological features are shown in A.

Figure 3. An overview of the Snøhvit 3D seismic data. A: Seismic bathymetry of the two datasets, B: Seismic inline example of Snøhvit 2011 (baseline) and C: seismic inline example of Snøhvit 2013 data (monitor). D: Amplitude spectra of the two datasets.

Figure 4. P-Cable 3D seismic data volumes acquired on the Vestnesa Ridge in 2012 (above) and 2013 (below). A: The seismic seafloor with the active pockmarks marked with names. B: The Vestnesa 2012 (baseline) and C: The Vestnesa 2013 data (monitor). D: amplitude spectrum of both datasets.

Figure 5. Schematic diagram of the P-Cable 3D Seismic system (Petersen et al. 2010). We use 14 streamers attached to a cross cable, spanned by two paravanes and towed perpendicular to the sail direction.

Figure 6. 4D processing flow of Lyngen 2014 – 2012 showing a seismic difference, time-shift maps (TS), cross-correlation maps and NRMS after various processing step for the two units 1 and 2. Predictability is initially and finally demonstrated between 400 and 650 ms since there was not an option of horizon separation when generating such map. The final difference is after step 5. Average NRMS and predictability are also indicated in the three sub-areas 1-3 illustrated on the final difference example. All values listed are average measures within the correlation volume.

Figure 7. A: Seismic example of Lyngen 2012 filtered with different bandpass filters (inline 20, the area is shown in figure 6), and B: corresponding final seismic difference example and NRMS values of unit 1 and 2. C: amplitude spectrum of the different bandpass-filtered Lyngen 214 and Lyngen 2012 as a reference for comparison. The best repeatability values are achieved with a narrow bandpass filter centered on dominant frequency (50-70-175-230 Hz).

Figure 8. 4D processing flow of Snøhvit 2013-2011 with processing parameters. The left column shows seismic difference after various processing steps and average repeatability measures of the window between 440 and 740 ms TWT. The right column show corresponding time-shift, predictability and NRMS maps of interval 1 (440-590 ms) and interval 2 (590-740 ms TWT). Step 5 predictability maps are draped with coherence map of Snøhvit 2011 of the two intervals to indicate poorer repeatability due to lack of continuity in reflections.

Figure 9. Seismic difference and repeatability measures between Vestnesa 2013 and Vestnesa 2012 during 4D processing. Seismic difference example (location in uppermost TS map) and Time Shift (TS), Predictability and NRMS map between time-window 1640-1850 ms two-way time after each 4D processing step. Values are average repeatability measures of the volumes. In addition, step 3 and 5 include TS map, and average values are presented between 1820 and 1950 ms TWT.

Figure 10. Reflective energy/noise in the water-column at Vestnesa 2012 and 2013 as shot noise (multiple energy from previous shot) and potentially side-scatter effect due to seafloor topography.

Figure 11. Stacked inline (un-migrated) of Lyngen 2012 and 2014 and seismic difference of migrated Lyngen 2014-2012. In the lower right corner, diffractions drawn from the two seismic inlines drapes the difference anomalies that are enhanced by illumination.

Figure 12. Final seismic difference between Vestnesa 2012 and 2013 (location presented in figure 4) in the Lunde-Lomvi area and echosounder data showing location of methane bubbles in the water-column. RMS amplitude anomaly map at two intervals (RMS 1 and 2) show how the 4D anomalies appear laterally.

Figure 13. A Seismic example of Vestnesa 2012 and 2013 (before and after 4D processing) and corresponding difference beneath the NE side of the Torsk pockmark and individual interpretation of fractures/small faults. In the column to the left, interpretation is overlaid the seismic difference, highlighting the 4D anomalies.

Figure A-1. F-K spectrum of (A) Inline 51 of Lyngen 2014, and same of (B) a zoom in around moraine ridge area (area to the right of figure) and of (C) a corresponding seismic difference (entire inline 51) indicating that 4D anomalies occur more frequently between 100 and 200 Hz, and in scattered dip-orientations. Horizontal lying reflections are well matched. 10 % of the lowest seismic difference amplitudes are here regarded as "background noise" and clipped off in front of the F-K analysis to visualize this effect.

LIST OF TABLES

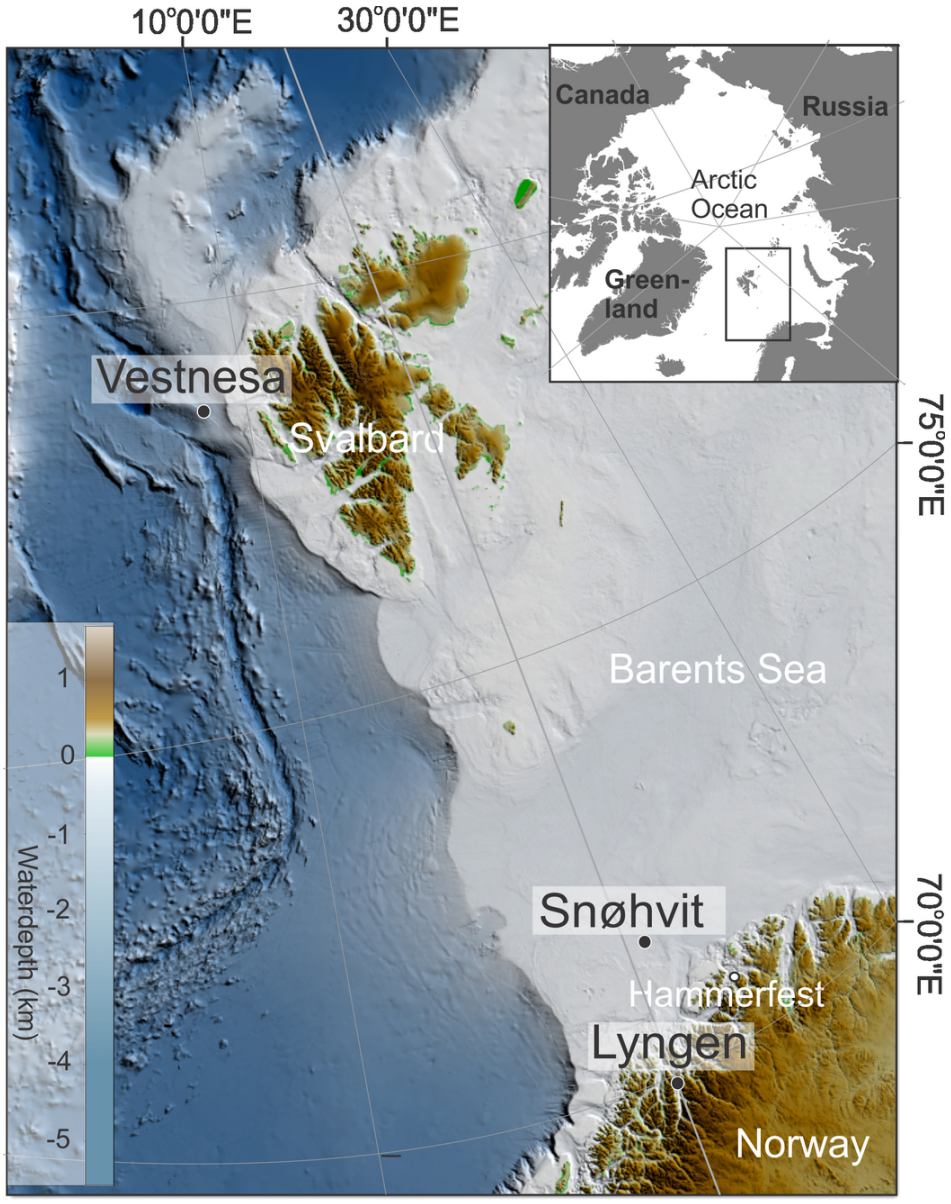

Figure 1. Overview map, showing the location of the different P-Cable seismic 4D survey sites, the Lyngen area, the Snøhvit area and the Vestnesa ridge.

88x112mm (300 x 300 DPI)

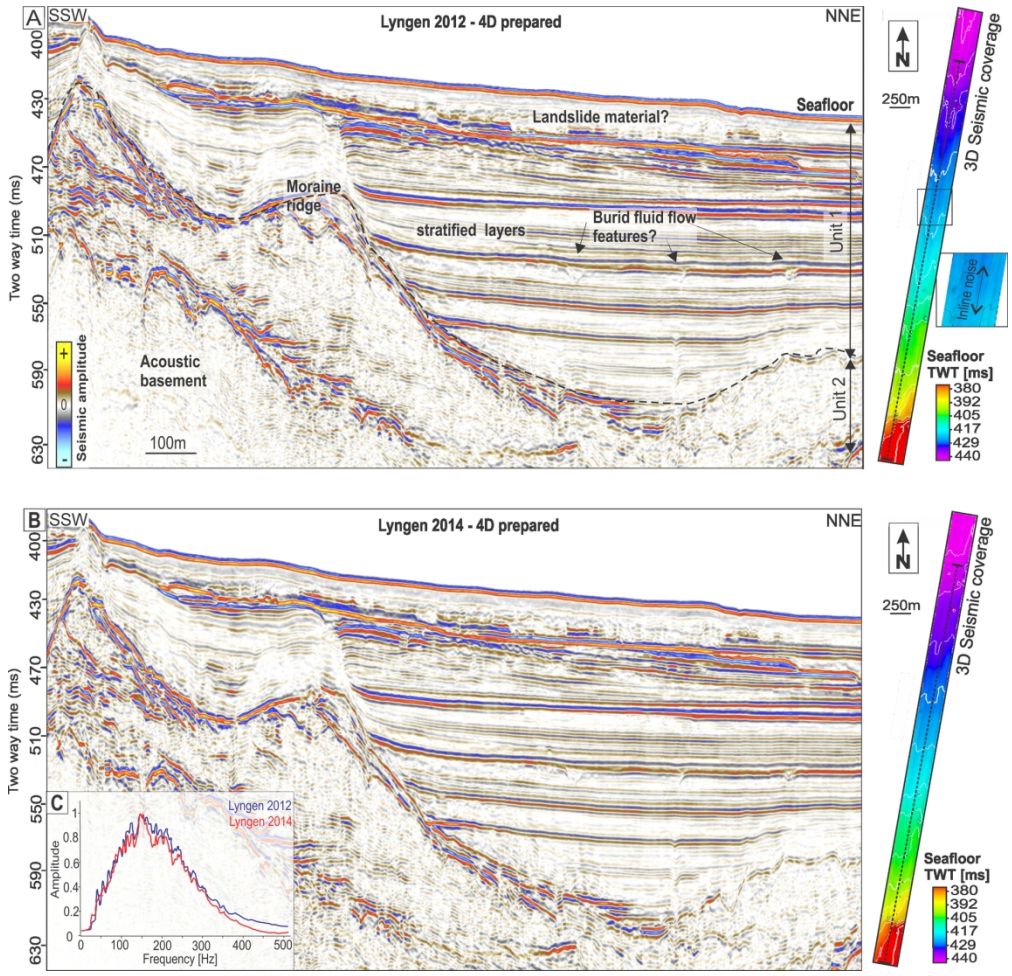

Figure 2. Seismic bathymetry (indicating seismic coverage) and inline example of the Lyngen 2012 and 2014 data. A: Lyngen 2012 (baseline) and B: Lyngen 2014 (monitor). C: Amplitude spectra of the two datasets. The main geological features are shown in A.

167x161mm (300 x 300 DPI)

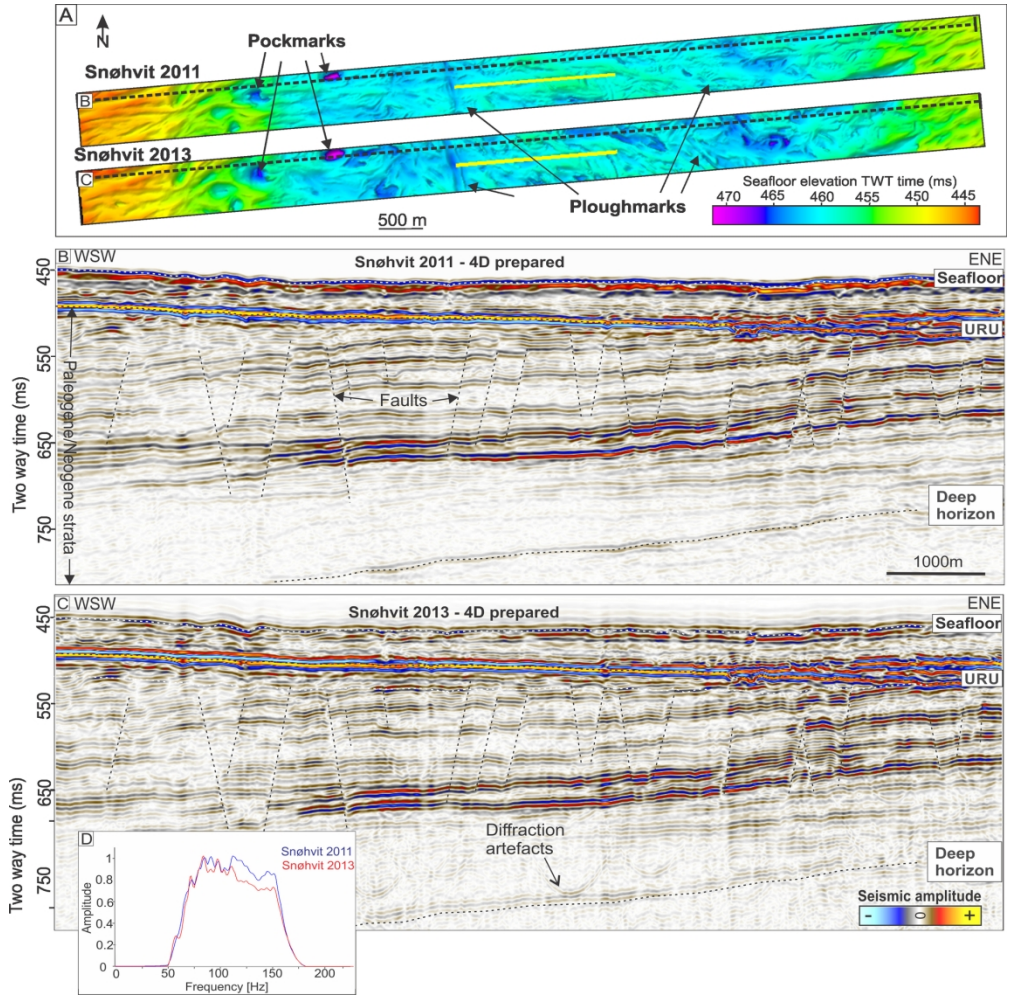

Figure 3. An overview of the Snøhvit 3D seismic data. A: Seismic bathymetry of the two datasets, B: Seismic inline example of Snøhvit 2011 (baseline) and C: seismic inline example of Snøhvit 2013 data (monitor). D: Amplitude spectra of the two datasets.

173x171mm (300 x 300 DPI)

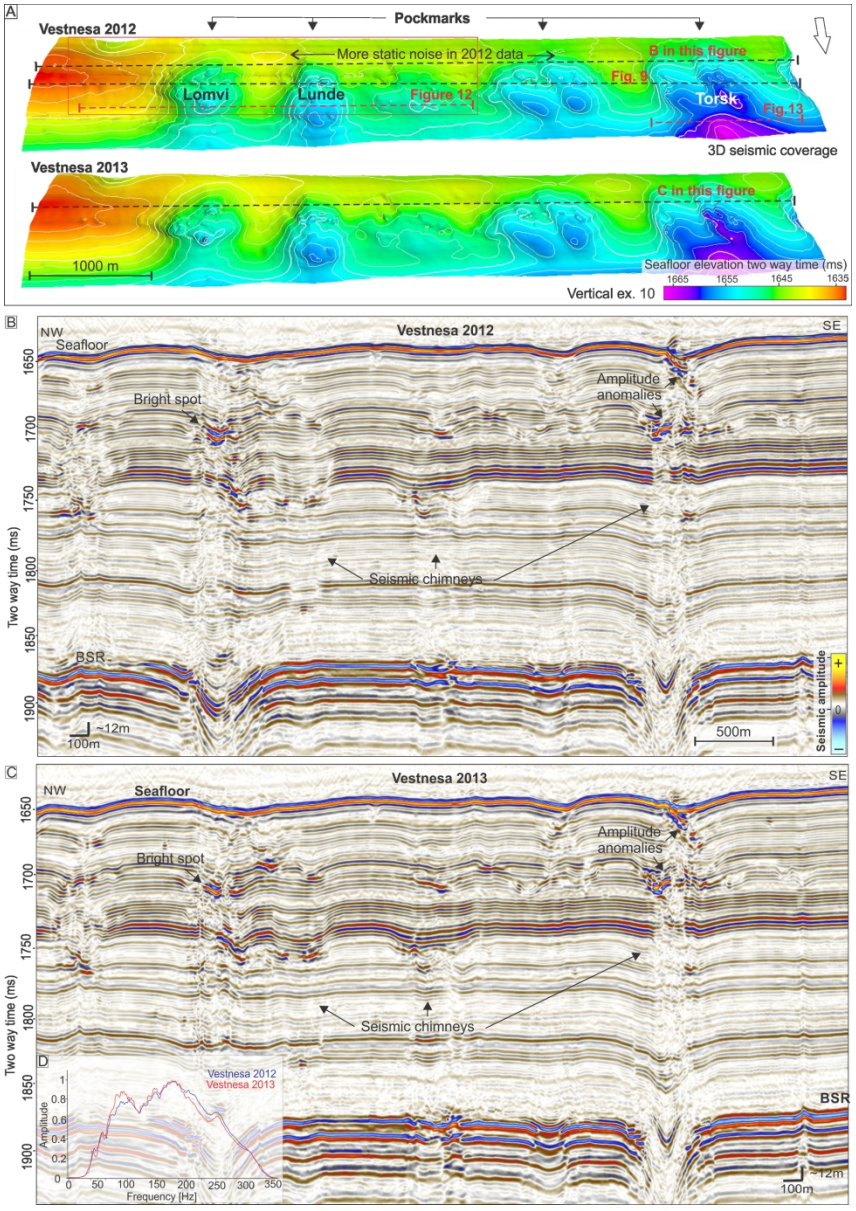

Figure 4. P-Cable 3D seismic data volumes acquired on the Vestnesa Ridge in 2012 (above) and 2013 (below). A: The seismic seafloor with the active pockmarks marked with names. B: The Vestnesa 2012 (baseline) and C: The Vestnesa 2013 data (monitor). D: amplitude spectrum of both datasets.

169x239mm (300 x 300 DPI)

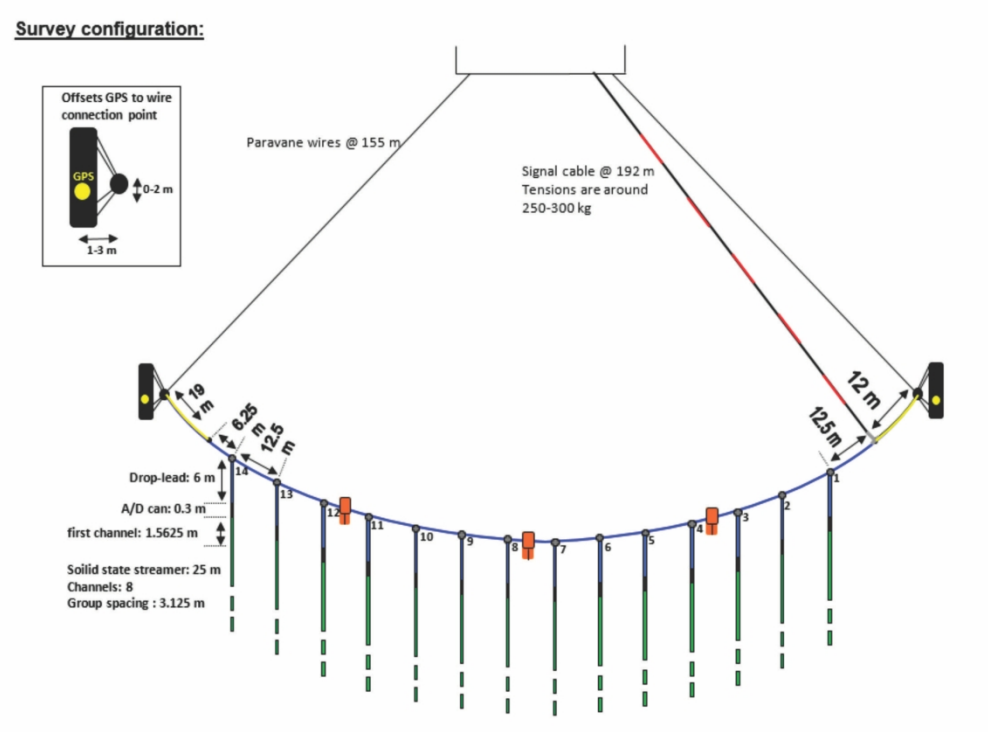

Figure 5. Schematic diagram of the P-Cable 3D Seismic system (Petersen et al. 2010). We use 14 streamers attached to a cross cable, spanned by two paravanes and towed perpendicular to the sail direction.

187x137mm (300 x 300 DPI)

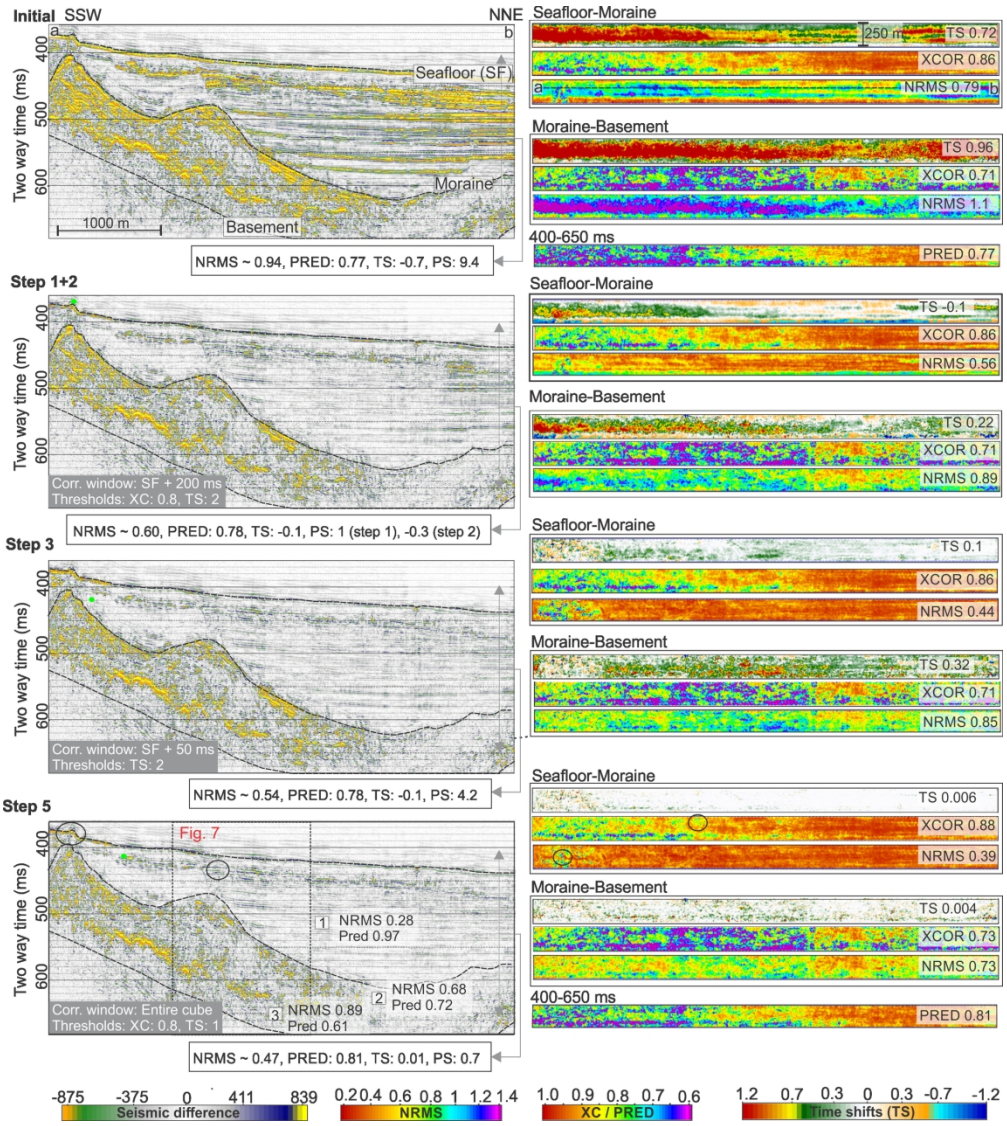

Figure 6. 4D processing flow of Lyngen 2014 – 2012 showing a seismic difference, time-shift maps (TS), cross-correlation maps and NRMS after various processing step for the two units 1 and 2. Predictability is initially and finally demonstrated between 400 and 650 ms since there was not an option of horizon separation when generating such map. The final difference is after step 5. Average NRMS and predictability are also indicated in the three sub-areas 1-3 illustrated on the final difference example. All values listed are average measures within the correlation volume.

175x195mm (300 x 300 DPI)

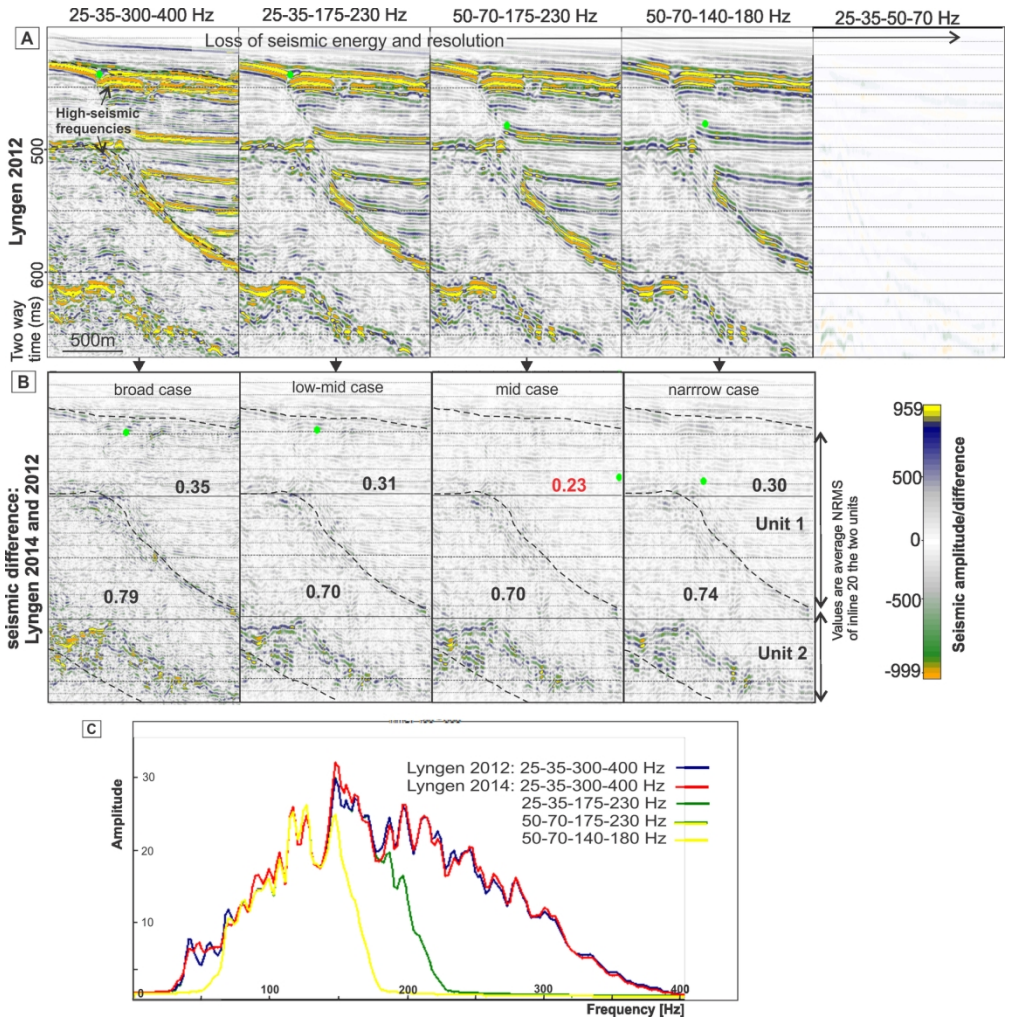

Figure 7. A: Seismic example of Lyngen 2012 filtered with different bandpass filters (inline 20, the area is shown in figure 6), and B: corresponding final seismic difference example and NRMS values of unit 1 and 2. C: amplitude spectrum of the different bandpass-filtered Lyngen 214 and Lyngen 2012 as a reference for comparison. The best repeatability values are achieved with a narrow bandpass filter centered on dominant frequency (50-70-175-230 Hz).

157x158mm (300 x 300 DPI)

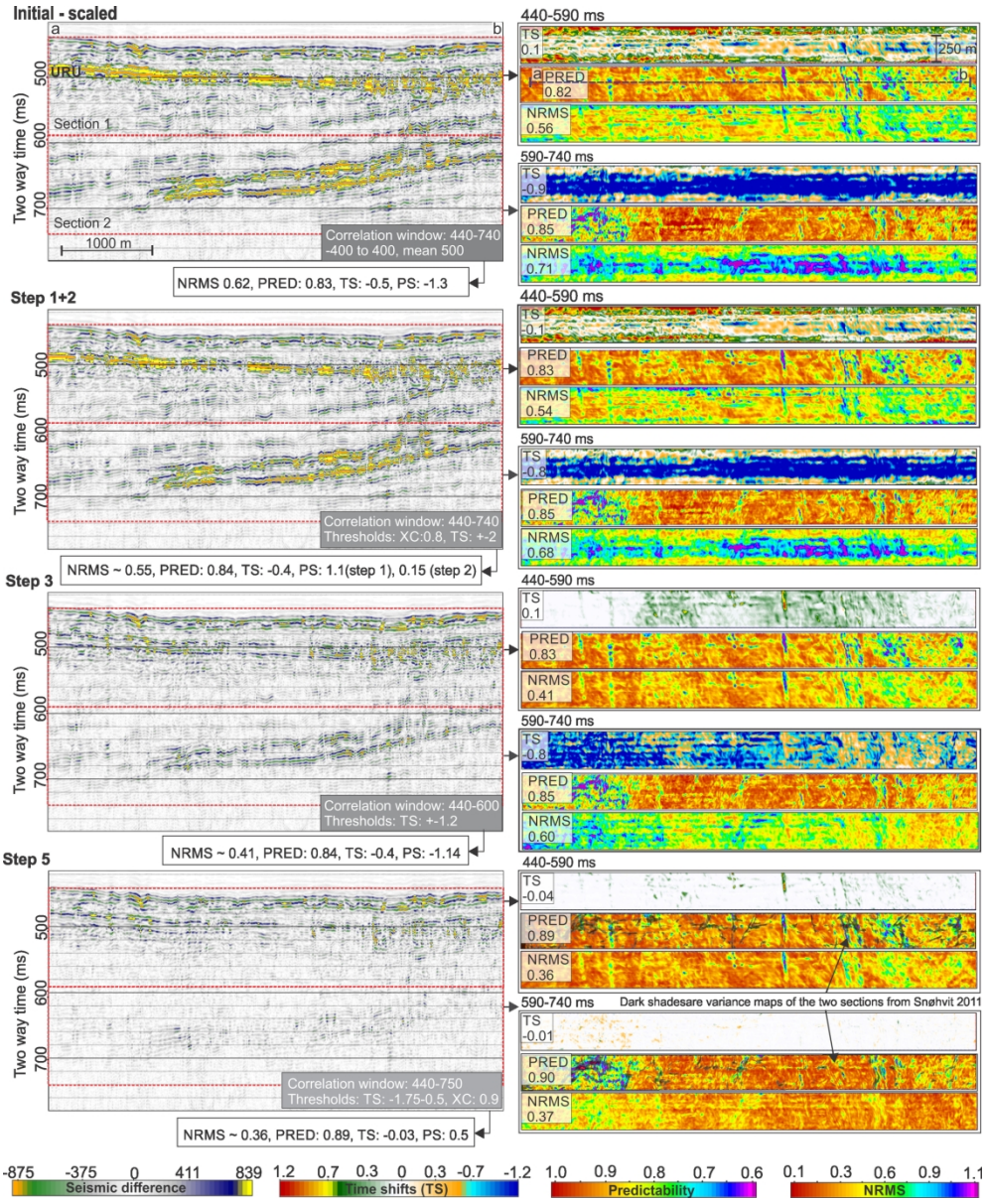

Figure 8. 4D processing flow of Snøhvit 2013-2011 with processing parameters. The left column shows seismic difference after various processing steps and average repeatability measures of the window between 440 and 740 ms TWT. The right column show corresponding time-shift, predictability and NRMS maps of interval 1 (440-590 ms) and interval 2 (590-740 ms TWT). Step 5 predictability maps are draped with coherence map of Snøhvit 2011 of the two intervals to indicate poorer repeatability due to lack of continuity in reflections.

176x214mm (300 x 300 DPI)

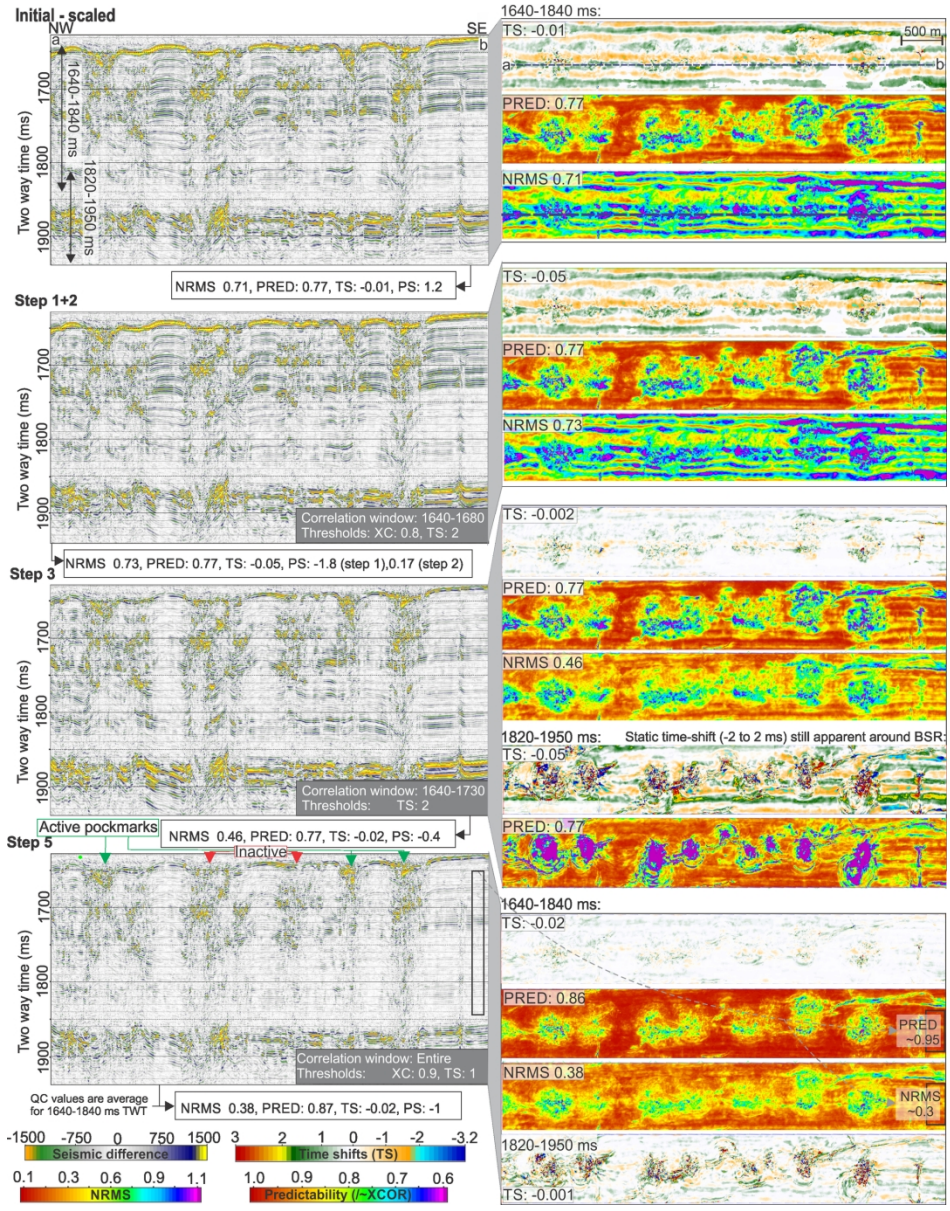

Figure 9. Seismic difference and repeatability measures between Vestnesa 2013 and Vestnesa 2012 during 4D processing. Seismic difference example (location in uppermost TS map) and Time Shift (TS), Predictability and NRMS map between time-window 1640-1850 ms two-way time after each 4D processing step. Values are average repeatability measures of the volumes. In addition, step 3 and 5 include TS map, and average values are presented between 1820 and 1950 ms TWT.

175x223mm (300 x 300 DPI)

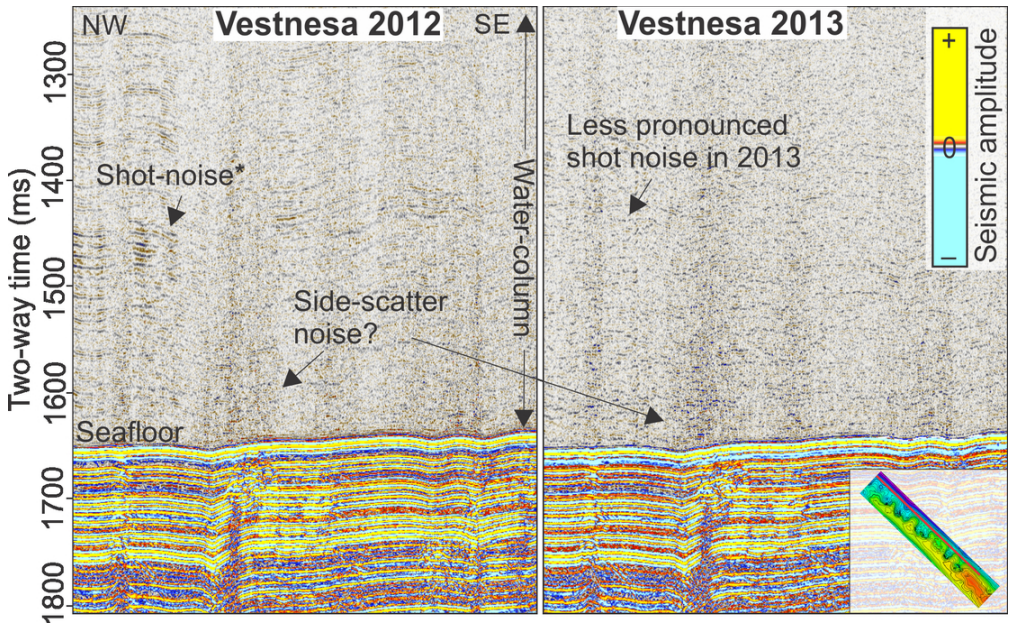

Figure 10. Reflective energy/noise in the water-column at Vestnesa 2012 and 2013 as shot noise (multiple energy from previous shot) and potentially side-scatter effect due to seafloor topography.

94x57mm (300 x 300 DPI)

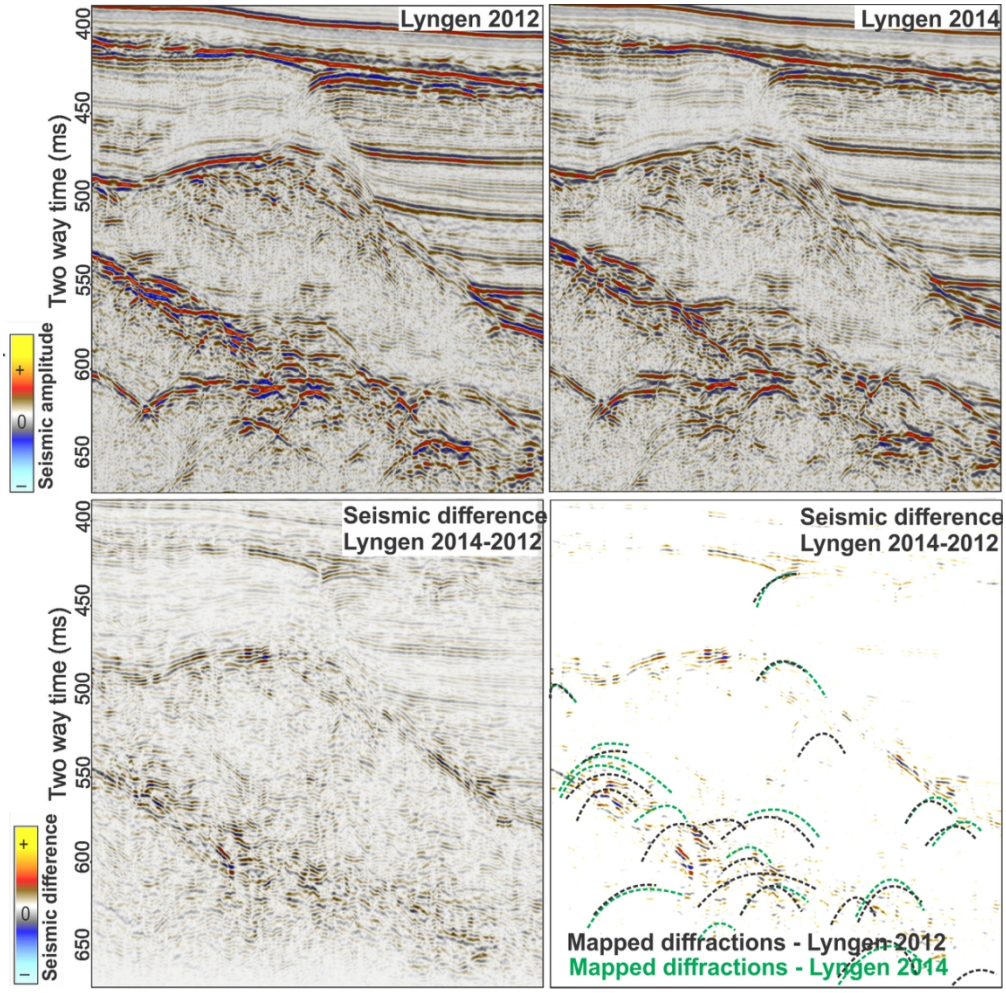

Figure 11. Stacked inline (un-migrated) of Lyngen 2012 and 2014 and seismic difference of migrated Lyngen 2014-2012. In the lower right corner, diffractions drawn from the two seismic inlines drapes the difference anomalies that are enhanced by illumination.

106x104mm (300 x 300 DPI)

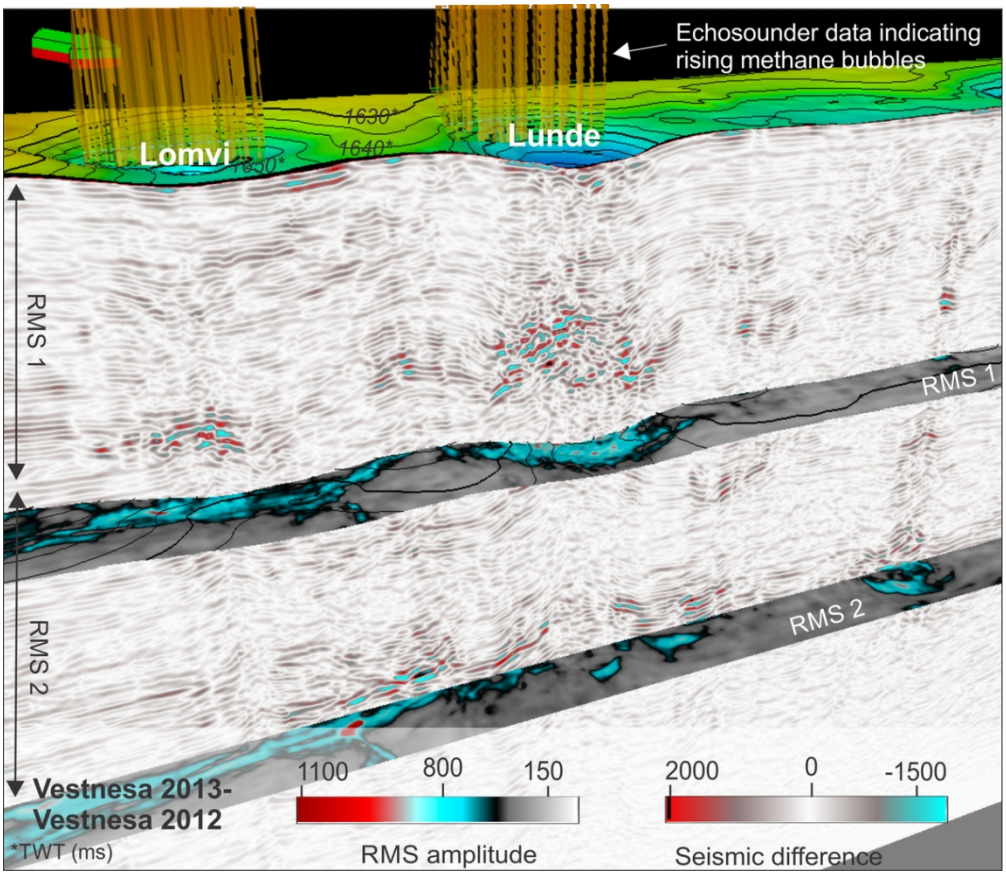

Figure 12. Final seismic difference between Vestnesa 2012 and 2013 (location presented in figure 4) in the Lunde-Lomvi area and echosounder data showing location of methane bubbles in the water-column. RMS amplitude anomaly map at two intervals (RMS 1 and 2) show how the 4D anomalies appear laterally.

102x88mm (300 x 300 DPI)

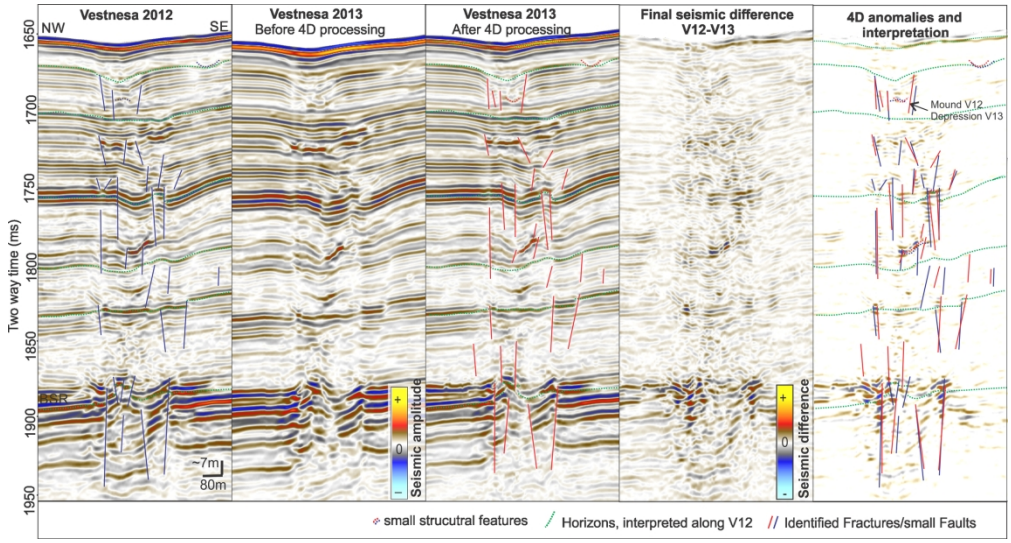

Figure 13. A Seismic example of Vestnesa 2012 and 2013 (before and after 4D processing) and corresponding difference beneath the NE side of the Torsk pockmark and individual interpretation of fractures/small faults. In the column to the left, interpretation is overlaid the seismic difference, highlighting the 4D anomalies.

201x107mm (300 x 300 DPI)

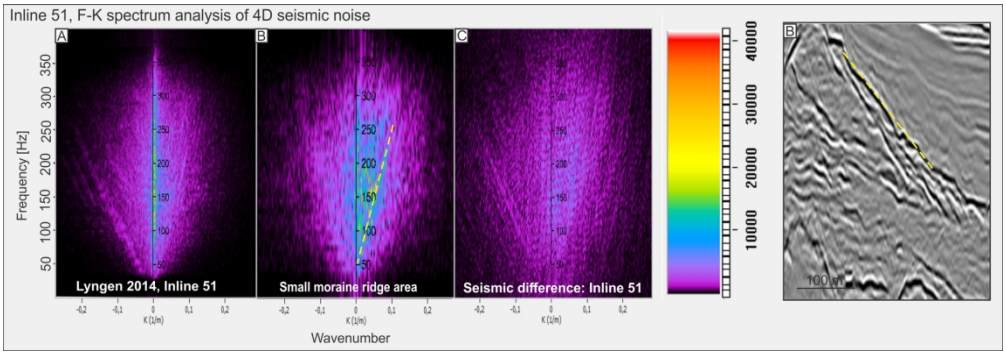

Figure A-1. F-K spectrum of (A) Inline 51 of Lyngen 2014, and same of (B) a zoom in around moraine ridge area (area to the right of figure) and of (C) a corresponding seismic difference (entire inline 51) indicating that 4D anomalies occur more frequently between 100 and 200 Hz, and in scattered dip-orientations. Horizontal lying reflections are well matched. 10 % of the lowest seismic difference amplitudes are here regarded as "background noise" and clipped off in front of the F-K analysis to visualize this effect.

158x55mm (300 x 300 DPI)

		Lyngen		Snøhvit		Vestnesa	
		2012	*2014*	*2011*	*2013*	*2012*	*2013*
Acquisition information	Acquisition lines	15	13	30	19	25	25
	Geometry deviation	<5 m	< 5 m	<5 m	<5m	<5m	<5 m
	Gun system	mini-GI (15/15 in^3)	mini-GI (15/15 in^3)	mini-GI (15/15 in^3)	mini-GI (15/15 in^3)	mini-GI (15/15 in^3)	mini-GI (15/15 in^3)
	Shooting pressure	160 bar	160 bar	160 bar	160 bar	170 bar	170 bar
	Shooting interval	4 sec	3 sec	4 sec	4 sec	4 sec	5-6 sec
	Streamer depth	1-2 m	1-2 m	1-2 m	1-2 m	1-2 m	1-2 m
	Weather (wind,, water temperature)	5-12 m/s form W-SW, 0-4 □	0-3 m/s form S. Calm sea	6-8 m/s, ~7.3 □	6-12 m/s, ~10□	4-12 m/s, 0-4 □	1.4-7 m/s, 5.5-6.5 □
	Area	3.3 km`2		2.4 km`2			10.7 km`2
	Inlines/Crosslines	1668/42		103/1061			151/861
Geometry	Binning	6.125x6.125	6.125x6.125	6.125x6.125	6.125x6.125	6.125x6.125	6.125x6.125
	Tides	Yes	Yes	Yes	Yes		
	Bandpass	10-30-380-500	10-30-380-500	5-10-350-380	5-10-350-380	30-50-300-350	30-50-300-350
	Amplitude correction	Spherical Divergence	Spherical Divergence	Spherical Divergence	Spherical Divergence	Spherical Divergence	Spherical Divergence
3D Processing workflow	NMO	1477 m/s	1477 m/s	1500 m/s	1500 m/s	1500 m/s	1500 m/s
	Stacking	Yes	Yes	Yes	Yes	Yes	Yes
	Interpolation	6.25 m	6.25 m	6.25 m	6.25 m	6.25 m	6.25 m
	Migration	3D stolt, 1500 m/s	3D stolt, 1500 m/s	3D stolt, 1500 m/s	3D stolt, 1500 m/s	3D stolt, 1500 m/s	3D stolt, 1500 m/s

This study 4D preparation and processing flow	
3D seismic processing	Input of SEGD files Geometry assignment and filtering Removal of bad channels Tide corrections 3D Binning (6.25 x 6.25 m) Spherical divergence correction Band-pass filter NMO using a velocity of 1500 m/s Ensemble stacking Interpolation 3D Stolt migration
4D preprocessing	Cut seismic to overlap (SeisSpace). Redefine geometry to common CDPs, Inlines and Crosslines (SeisSpace). Bulk shift repeat to match reference using seafloor mean (Petrel). Phase shift if repeat and reference are of reverse polarity compared to each other (Petrel). Noise attenuation (GeoTeric). Rescaling seismic amplitudes of repeat and reference to a common average using a mean RMS of 500 (HRS Pro4D).
4D processing	1)Phase and time correction: global 2) Matching filter phase and amplitude using a shaping filter: global and combined) 3) Time correction (no phase): trace-by-trace 4)Rescaling amplitudes: global 5) Time variant time shift correction: Precondition XC and TS. (HRS Pro4D)
4D Interpretation	Using seismic -difference cubes, modified repeat and reference seismic data. NRMS, predictability, time-shift volumes and slices. Investigating anomalies in chimneys and along the BSR.

Method	What it does
Global phase and time correction	Applies a global or average bulk and phase-shift of the monitor survey to better vertically align the time and phase to the base.
Matching filter phase and amplitude using a shaping filter	A global frequency bandwidth and phase shaping filter applied to the monitor survey to match those with the base.

Trace-by trace time and phase correction	Correct for misalignments in time (and phase if chosen) between monitor and base surveys because of shallow static differences (e.g., differences in sea level).
Rescaling amplitudes	Normalizes the amplitudes if not in balance (if RMS factor is not close to 1) using a new scalar from the base survey.
Time variant time shift correction	Compensates and corrects for differences in travel time of reflection events, caused by a stretch in the data and velocity changes due to nearby fluid/gas areas.

	Lyngen	Snøhvit	Vestnesa
Acqusition			
Time of year	2012: 5-6th of May 2014: 12-13th of April	2011: 3-5th of July 2013: 12-13th of July	2012: 19-24th of June 2013: 17-19th of July
Sailing speed (knots):	2012: ~4.3 2014: No data	2011: ~4.5 2013: ~4.5	2012: ~4 2013: ~3.5
Vessel noise	Probably same level of vibrations since the same vessel is used for both surveys	Probably same level of vibrations since the same vessel is used for both surveys	Probably same level of vibrations since the same vessel is used for both surveys
Position accuracy	<5 m	<5 m	<5 m
Gun signature	Identical Pressure (160 bar), gun depth (2 m) and type (1 15 inch^3 GI-mini airgun)	Identical Pressure (160 bar), gun depth (2 m) and type (1 15 inch^3 GI-mini airgun)	Identical Pressure (170 bar), gun depth (2 m) and type (1 15 inch^3 GI-mini airgun)
Shot interval	2012: 4 sec 2014: 3 sec	2011: 4 sec 2013: 4 sec	2012: 4 sec 2013: 5-6 sec
Wind	2012: 5-12 m/s 2014: 0-3 m/s	2011: 6-8 m/s 2013: 6-12 m/s	2012: 4-12 m/s 2013: 1.4-7 m/s
Water temperature	2012: 0-4□ 2014: No data	2011: ~7.3□ 2013: ~10□	2012:0-4□ 2013: 5.5-6-5□
Water multiples	Seismic below first multiple so insignificant	Seismic below first multiple so insignificant	Seismic below first multiple so insignificant
Side-scatter effect	Not visible	Not visible	Possible related to pockmarks
Preparation and processing	Side-by-side (identical)	Side-by-side (identical)	Side-by-side (identical)
Geology			
Seabed topography	Gentle	Rough due to plough-marks	Somewhat rough around pockmarks
Complexity of overburden	Poor repeatability at and below moraine ridge	Seafloor and URU	
Diffraction phenomena	Intense at and below moraine ridges	URU and seafloor	Seafloor pockmarks, chimneys, faults and from BSR
Seismic penetration	Low beneath moraine ridge	Low beneath 650 ms TWT	Good
S/N just beneath seafloor	2012: 57 2014: 55.7	2011: 31.5 2013: 43	2012: 12.9 2013: 18.7
FOLD (average)	2012: 13 2014: 14	2011: 7 2013: 11.5	2012: 8.7 2013: 7.2
Average seafloor depth (ms TWT) **Difference (ms)**	2012: 386.9 2014: 388.6 1.7 ms	2011: 454.8 2013: 456.9 2.1 ms	2012: 1649.37 2013: 1648.39 ~1 ms (0.735 m)

DATA AND MATERIALS AVAILABILITY

Data associated with this research are available and can be obtained by contacting the corresponding author.